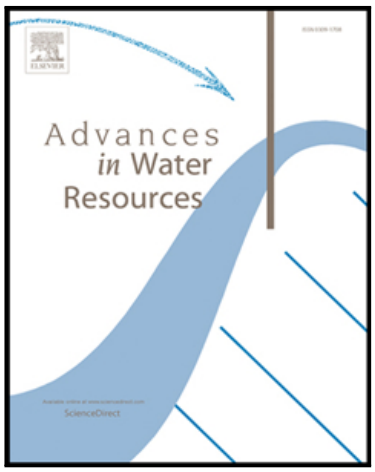

Flood inundation modelling in urbanized areas: a mesh-independent porosity approach with anisotropic friction

ALESSIA FERRARI , DANIELE P. VIERO , RENATO VACONDIO , ANDREA DEFINA , PAOLO MIGNOSA

PII: S0309-1708(18)30604-3
DOI: https://doi.org/10.1016/j.advwatres.2019.01.010
Reference: ADWR 3272

To appear in: *Advances in Water Resources*

Please cite this article as: ALESSIA FERRARI , DANIELE P. VIERO , RENATO VACONDIO , ANDREA DEFINA , PAOLO MIGNOSA , Flood inundation modelling in urbanized areas: a mesh-independent porosity approach with anisotropic friction, *Advances in Water Resources* (2019), doi: https://doi.org/10.1016/j.advwatres.2019.01.010

Highlights

- A GPU accelerated SWE numerical scheme with porosity is presented
- The proposed approach guarantees mesh independence for structured grids
- Anisotropic friction source term based on porosity conveyance is introduced
- Friction source term is expressed in tensor form
- The proposed formulation guarantees the *C-property*

Flood inundation modelling in urbanized areas: a mesh-independent porosity approach with anisotropic friction

ALESSIA FERRARI, PhD, Research Assistant, *Department of Engineering and Architecture, University of Parma, Parco Area delle Scienze 181/A, 43124 Parma, Italy*

Email: alessia.ferrari@unipr.it

DANIELE P. VIERO, PhD, Research Fellow, *Department of Civil, Environmental and Architectural Engineering, University of Padova, via Loredan 20, 35131 Padova, Italy*

Email: daniele.viero@unipd.it

RENATO VACONDIO, PhD, Research Fellow *Department of Engineering and Architecture, University of Parma, Parco Area delle Scienze 181/A, 43124 Parma, Italy*

Email: renato.vacondio@unipr.it

ANDREA DEFINA, PhD, Full Professor, *Department of Civil, Environmental and Architectural Engineering, University of Padova, via Loredan 20, 35131 Padova, Italy*

Email: andrea.defina@dicea.unipd.it

PAOLO MIGNOSA, PhD, Full Professor, *Department of Engineering and Architecture, University of Parma, Parco Area delle Scienze 181/A, 43124 Parma, Italy*

Email: paolo.mignosa@unipr.it

Abstract

In the present work, a porosity-based numerical scheme for the Shallow Water Equations is presented. With the aim of accounting for the presence of storage areas, such as gardens, yards and dead zones, and for preferential flow pathways, both an isotropic storage porosity parameter and anisotropic friction are adopted. Particularly, the anisotropic effects due to the building alignments are evaluated defining conveyance porosities along principal directions and using them to express the friction losses in tensor form. The storage and conveyance porosities are evaluated from the geometry of the urban layout at a district scale and then assigned to computational cells rather than to cell sides, thus avoiding oversensitivity to the mesh design. The proposed formulation guarantees the *C-property* also in presence of wet-dry fronts. Model testing is performed analyzing schematic and idealized urban layouts, and against experimental data as well. The results obtained by the proposed anisotropic scheme are similar to a high-resolution model with resolved buildings, also in the presence of low-friction regimes, meanwhile with a remarkable reduction of the computational times.

Introduction

Two-dimensional Shallow Water Equations (2D-SWEs) are widely adopted to model flood propagation, inundations, dam breaks, and many different accurate and robust numerical schemes have been developed to simulate supercritical, subcritical and transient flows with shocks and hydraulic jumps that may occur dealing with real irregular bathymetries.

In large-scale urban inundation modelling, the use of subgrid models allows upscaling the SWEs, so as to account for effects exerted by buildings, curbs, walls, and other small-scale features at an affordable computational cost [1–4]. Indeed, the solution of the classical SWEs on suitably refined grids, i.e., on grids allowing to capture localized flow features, is still a challenge due to the large extent of urban areas and to the extremely different spatial scales involved in inundation processes [5,6]. In such cases, the presence of buildings and small-scale obstacles can be accounted for using porosity-based subgrid models, which significantly reduce the need of computational resources [3,4]. Several studies have shown that the use of porosity is the most effective approach in macroscopic modelling of urban floods [1,2,7–10].

The use of artificial porosity was introduced more than twenty years ago to account for subgrid-scale topographic effects in modelling inundation flows using the SWEs [11,12], and river flows based on the Reynolds-Averaged Navier-Stokes Equations [13]. Guinot and Soares-Frazão [14] formalized the so-called Single Porosity (SP) model for inundation flows in urban areas, in which the porosity reflects the geometrical properties of the medium, and suitable coefficients are introduced to cope with head losses due to the urban singularities.

Since then, several significant contributions on porosity-based Shallow Water models have appeared in the literature [15–22]. One of the most effective and promising is the Integral Porosity (IP) formulation [23] that upscales the SWEs in integral form, so as to release the hypothesis of continuum medium that are implicitly assumed when the basic equations are expressed in differential form. In addition, two different kinds of porosity are introduced: the isotropic storage porosity, representing the volume fraction available for mass and momentum storage, and a conveyance porosity, accounting for the connectivity of the urban medium. The distinction between storage and conveyance porosities leads to a better description of the flow field than in the SP model. Importantly, the use of a conveyance porosity allows capturing the anisotropic effects that commonly arise in real urban layouts, where obstacles and topography can significantly affect the flow direction [1,8,23–25].

The IP model has been the object of numerous applications and further enhancements [26–30]. Guinot et al. [4] recently improved the IP model from both a theoretical and practical point of views

[31]; in their Dual Integral Porosity (DIP), the distinction between storage and conveyance porosities is better formalized, and simple closure relations are introduced to link them together. As a result, only the storage porosity appears in the continuity equation, in agreement with previous findings [32].

Unfortunately, the IP and DIP models suffer from an unusual sensitivity to the computational grid [33]. This partly descends from the fact that the conveyance porosity is defined locally at the edges of the computational cells [23]; intersections between cell sides and building footprint change significantly, even for relatively small rearrangements of the mesh [29]. This problem can be limited by adopting suitable unstructured grids [10,23]. Nevertheless, oversensitivity to the mesh design is also due to a polarization of fluxes that emerges when the flux porosity field is anisotropic [33], and makes numerical solutions to depend on cell edge orientation (not only on its location). Mesh design guidelines are provided in [33]; their fulfilment is not trivial in real-world applications when using unstructured meshes, and is obviously impossible when using Cartesian structured grids.

According to Guinot [33], mesh dependency can be reduced by providing a better description of the connectivity porosity field, with an approach that reflects the connectivity properties of the urban medium *within the cells* and not only at the cell interfaces.

In response to this need, the present paper explores a new, simple porosity approach with anisotropic friction. The effects exerted by buildings are accounted for using an isotropic porosity for storage reduction and anisotropic friction for reduced conveyance and alteration in the flow direction. Friction is evaluated in tensor form based on directionally dependent conveyance porosity parameters. The porosity parameters are geometrically evaluated on suitable portions of the urban layout. As a result, they are not influenced by the mesh design and thus the proposed scheme can be adopted in numerical models based on structured grids. The anisotropic friction losses are then introduced in a well-balanced formulation solving the 2D-SWEs with porosity. Despite well balanced schemes were presented also in previous works [14,15,23 among the others], in the present paper the formulation of Liang and Borthwick [34] is extended to the porous 2D-SWEs, and, thus, the *C-property* is preserved also in presence of wet-dry fronts, regardless the slope source term discretization. The subgrid model for building treatment, which is described in Sect. 1, is implemented within the framework of the PARFLOOD 2D Finite Volume model [35–38], which solves the SWEs on efficient Cartesian and non-uniform structured grids using a GPU-enhanced, parallel solver (described in Sect. 2). The model is tested both through idealized schematic

applications and against experimental data (Sect. 3), in order to highlight the model skills and the needs for future improvements.

1. A porosity approach for anisotropic urban layouts

The presence of buildings has a threefold effect on the flow field in urban areas: (i) it reduces mass and momentum storage within ponded areas, (ii) it causes a concentration of fluxes in constrained pathways, thus locally increasing the velocity and creating recirculation and/or dead zones, and (iii) it alters the flow directions.

The first effect is taken into account by introducing the storage, isotropic porosity ϕ in both the continuity and momentum equations [14]. The second effect entails additional resistances to the flow; commonly, it is accounted for by expressing friction in terms of effective flow velocities and by adding drag coefficients in various forms [14,31,39]. The third effect is evaluated, in IP and DIP approaches, by defining conveyance porosities on cell edges based on the footprint method [4,23], and also by expressing the drag coefficients in tensor form, so as to make them dependent on flow direction [4,39].

Specifically, in IP and DIP models, conveyance porosities are locally (i.e., point-based) evaluated, and they are only used in computing flux variables at the cell edges [4,23]. Such flux variables are typically provided by Riemann solvers that work under the hypothesis of inviscid flow [18,19,40,41], thus neglecting flow resistance, as well as the connectivity of the urban medium within the adjacent cells [33].

The key idea of the present paper is to consider conveyance porosities, which are geometrically calculated from the urban layout, to evaluate friction and drag losses in the SWEs. Resistances exerted by buildings and obstacles can be ascribed to different mechanisms, such as hydrostatic pressure forces, advective accelerations, flow separation, (transient) momentum exchanges, shock-wave reflections [33,42–45]. Importantly, the presence of (often aligned) buildings also acts to concentrate the flow into narrower cross-sections that, for a given discharge, implies far greater head losses due to increased velocity. This effect is well reflected by the concept of conveyance porosity, which expresses the fraction of cross-sectional area available to flow in a given direction. The introduction of anisotropic resistances as a function of conveyance porosity, in addition to the isotropic storage porosity, also allows describing the presence of storage yards and other stagnant areas, which generate the so-called dead zones [23,45]. Moreover, the undesired mesh-dependence

of the IP and DIP models is avoided by evaluating porosity parameters on suitable portions of the urbanized area and by assigning them to computational elements rather than to cell sides.

A similar modeling approach, which although introduces conveyance porosity in evaluating not only friction terms, but also advective accelerations, has been successfully implemented in a Finite Element, semi-implicit, mixed Eulerian/Lagrangian model based on staggered unstructured triangular meshes [46]. However, the model in [46] is neither suitable to deal with supercritical or rapidly varying flows, nor with shock waves, i.e., flow conditions that are not uncommon in urban floods.

In the proposed approach, the first effect exerted on the flow field by buildings (i.e., reduction in mass and momentum storage) is assessed by means of a storage isotropic porosity analogously to the SP, IP, and DIP models. The second and the third effects (i.e., modification of velocity field in terms of magnitude and direction) are accounted for unitarily through a tensor formulation of friction based on conveyance porosity that is evaluated on suitable portions of urbanized area. In the present study, as a first attempt to model urban floods using a FV scheme with porosity-based anisotropic friction, porosity parameters are evaluated looking at the urban layout as a whole; district-scale evaluation of porosities has been adopted also in previous studies aimed at large-scale simulation of urban areas [20]. This choice is coherent with the schematic and quite uniform arrangement of urban districts used hereinafter to test the model.

Conveyance porosity is evaluated under a set of simplifying hypothesis; it is first introduced with respect to the one-dimensional (1-D) schematic framework. Looking at Figure 1-a, Q is the flow rate, W is the width of the computational element, and w is the width of the narrower cross-section, wherein the flow is constrained owing to the presence of buildings (shaded areas). The channel contraction is characterized by only one geometric parameter, namely the width ratio w/W [47], which is taken here as the conveyance porosity, Ψ. Denoting the water depth with h, the effective flow velocity u_e in the channel contraction is:

$$u_e = \frac{Q}{wh} = \frac{Q}{\Psi W h} \quad (1)$$

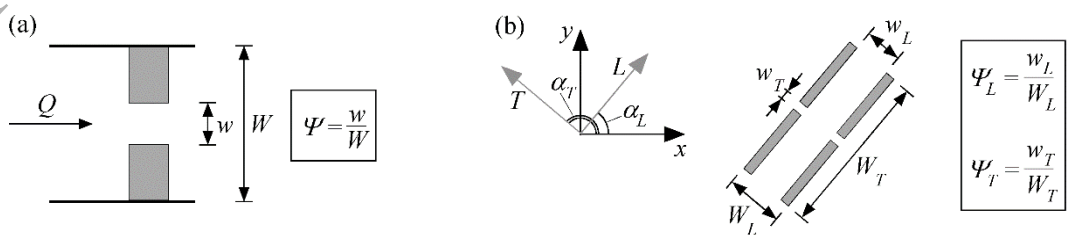

Figure 1. Definition of the conveyance porosity, Ψ, in a one-dimensional schematic example (a), and along principal directions (L-T) in a schematic two-dimensional example (b).

It has to be noted that, in the model formulation originally proposed by [14] and used in most of the following works on porosity-based models, the flow velocity (u) already takes into account the presence of buildings, which partly reduces the room available to flow, through the storage porosity, ϕ. The flow velocity, averaged over the entire computational element (i.e., including the area occupied by buildings), is thus $U = \phi u$. In the proposed porosity approach, friction losses are evaluated with reference to the flow velocity in the narrowest cross-section that is derived from Eq. (1) as:

$$u_e = \frac{UWh}{\Psi Wh} = \frac{\phi u}{\Psi} \quad (2)$$

This means that, when the conveyance porosity is equal to the storage porosity, the proposed model reduces to the SP model [14].

The concepts described above can be extended quite straightforwardly to a two-dimensional framework. To include anisotropic effects owing to roads and build alignment, which tend to convey the flow along preferential pathways, conveyance porosities are evaluated along principal directions, and friction terms are then introduced in SWEs solver in tensor form [48]. In the two-dimensional (2-D) example of Figure 1-b, two principal directions of maximum and minimum conveyance, namely L and T, can be easily identified. In Figure 1-b, the L and T directions are mutually orthogonal but, in general, α_T can differ from $\alpha_L \pm \pi/2$. Along each principal direction, conveyance porosities are evaluated by analogy with the 1D case, i.e., considering the ratio between the width of the narrowest cross-section and the total width. The implementation of the proposed anisotropic porosity approach in the friction term of a 2D-SWE solver will be explained in the next section.

The simplifying hypothesis that has been here assumed to assess resistance terms by means of conveyance porosity requires some further discussion. In fact, friction losses are evaluated referring to the velocity at the contraction and this corresponds assuming that water flows within the narrowest cross-section for the entire length of the computational grid. However, considering that friction losses vary linearly with the length of the path and quadratically with the velocity, most of the dissipation occurs where velocity is greater. In addition, due to the jet developing downstream of contractions, the higher velocities are sustained in the flow direction, so that the effective length of the narrowest section is longer than its purely geometrical length. The same hypothesis has been assumed also in other studies [7,16,27,46].

2. Numerical model

The anisotropic porosity approach described in Sect. 1 is implemented in a finite volume scheme solving the 2D Shallow Water Equations, which in the single porosity (SP) formulation are expressed as follows [14]:

$$\begin{cases} \dfrac{\partial}{\partial t}(\phi h)+\dfrac{\partial}{\partial x}(\phi uh)+\dfrac{\partial}{\partial y}(\phi vh)=0 \\ \dfrac{\partial}{\partial t}(\phi uh)+\dfrac{\partial}{\partial x}\left(\phi u^2h+\dfrac{1}{2}g\phi h^2\right)+\dfrac{\partial}{\partial y}(\phi uvh)=\dfrac{1}{2}gh^2\dfrac{\partial\phi}{\partial x}-g\phi h\dfrac{\partial z}{\partial x}-g\phi h\dfrac{n^2u_e\sqrt{u_e^2+v_e^2}}{h^{4/3}} \\ \dfrac{\partial}{\partial t}(\phi vh)+\dfrac{\partial}{\partial x}(\phi uvh)+\dfrac{\partial}{\partial y}\left(\phi v^2h+\dfrac{1}{2}g\phi h^2\right)=\dfrac{1}{2}gh^2\dfrac{\partial\phi}{\partial y}-g\phi h\dfrac{\partial z}{\partial y}-g\phi h\dfrac{n^2v_e\sqrt{u_e^2+v_e^2}}{h^{4/3}} \end{cases} \quad (3)$$

where ϕ represents the storage porosity, h the water depth, u and v the velocity in x and y-direction, u_e and v_e the effective flow velocity in the channel contraction along x and y axis, g the gravitational acceleration, z the bottom elevation, and n the Manning coefficient.

Following the idea of Cea and Vázquez-Cendón [15], the system of 2D-SWEs with porosity (3) can be further algebraically modified, by expanding the partial derivatives and assuming the porosity constant in time ($\partial\phi/\partial t=0$), continuous and differentiable in space. Thus, system (3) becomes:

$$\begin{cases} \dfrac{\partial h}{\partial t}+\dfrac{\partial}{\partial x}(uh)+\dfrac{\partial}{\partial y}(vh)=-\dfrac{h}{\phi}\left(u\dfrac{\partial\phi}{\partial x}+v\dfrac{\partial\phi}{\partial y}\right) \\ \dfrac{\partial uh}{\partial t}+\dfrac{\partial}{\partial x}\left(u^2h+\dfrac{1}{2}gh^2\right)+\dfrac{\partial}{\partial y}(uvh)=-\dfrac{uh}{\phi}\left(u\dfrac{\partial\phi}{\partial x}+v\dfrac{\partial\phi}{\partial y}\right)-gh\dfrac{\partial z}{\partial x}-gh\dfrac{n^2u_e\sqrt{u_e^2+v_e^2}}{h^{4/3}} \\ \dfrac{\partial vh}{\partial t}+\dfrac{\partial}{\partial x}(uvh)+\dfrac{\partial}{\partial y}\left(v^2h+\dfrac{1}{2}gh^2\right)=-\dfrac{vh}{\phi}\left(vh\dfrac{\partial\phi}{\partial x}+v\dfrac{\partial\phi}{\partial y}\right)-gh\dfrac{\partial z}{\partial y}-gh\dfrac{n^2v_e\sqrt{u_e^2+v_e^2}}{h^{4/3}} \end{cases} \quad (4)$$

The formulation in Eq. (4) presents the classical 2D-SWEs terms on the left hand-side and includes the porosity only by means of two non-conservative products on the right hand-side. It has to be noted that, while this formulation is correct for differentiable porosity fields, it may produce

unpredictable errors, which strongly depend on the numerical scheme, in the case of discontinuous porosity [49].

With the aim of preserving a well-balanced scheme also in presence of the 2D-SWEs with porosity, further manipulations are here performed in order to adopt the formulation of [34], which was introduced for the classical SWEs. The scheme allows the balance between fluxes and source terms, and guarantees the *C-property* regardless of the slope source term discretization, the approximate Riemann solver, and with wet-dry interfaces. Recalling the relation among water depth, bottom and water surface elevation $h=\eta-z$, system (4) can be written as:

$$\begin{cases} \dfrac{\partial \eta}{\partial t}+\dfrac{\partial}{\partial x}(uh)+\dfrac{\partial}{\partial y}(vh)=-\dfrac{h}{\phi}\left(u\dfrac{\partial \phi}{\partial x}+v\dfrac{\partial \phi}{\partial y}\right) \\ \dfrac{\partial uh}{\partial t}+\dfrac{\partial}{\partial x}\left(u^2h+\dfrac{1}{2}g(\eta^2-2\eta z)\right)+\dfrac{\partial}{\partial y}(uvh)=-\dfrac{uh}{\phi}\left(u\dfrac{\partial \phi}{\partial x}+v\dfrac{\partial \phi}{\partial y}\right)-g\eta\dfrac{\partial z}{\partial x}-gh\dfrac{n^2u_e\sqrt{u_e^2+v_e^2}}{h^{4/3}} \\ \dfrac{\partial vh}{\partial t}+\dfrac{\partial}{\partial x}(uvh)+\dfrac{\partial}{\partial y}\left(v^2h+\dfrac{1}{2}g(\eta^2-2\eta z)\right)=-\dfrac{vh}{\phi}\left(u\dfrac{\partial \phi}{\partial x}+v\dfrac{\partial \phi}{\partial y}\right)-g\eta\dfrac{\partial z}{\partial x}-gh\dfrac{n^2v_e\sqrt{u_e^2+v_e^2}}{h^{4/3}} \end{cases} \quad (5)$$

Analogously to system (4), the formulation in (5) has the advantage of considering the porosity by introducing non-conservative products in the continuity and in the two momentum equations, meanwhile preserving the adopted classical SWE scheme. Moreover, the derived system (5) is well balanced, since the only porosity-related terms are multiplied by the velocity, and they vanish in case of water at rest; thus, the remaining classical 2D-SWE scheme guarantees the *C-property*.

In the present work, the PARFLOOD 2D numerical model presented in [35–38] for the classical 2D-SWEs is adopted and modified for including the porosity-related source terms. The model solves in a finite volume scheme the following system of 2D-SWEs written in integral form [50]:

$$\frac{d}{dt}\int_A \mathbf{U}dA+\int_C \mathbf{H}\cdot\mathbf{n}\,dC=\int_A(\mathbf{S}_0+\mathbf{S}_f+\mathbf{S}_p)dA \quad (6)$$

where A denotes the area of the integration element, C the element boundary, $\mathbf{n}$ the outward unit vector normal to C, $\mathbf{U}$ the vector of the conserved variables and $\mathbf{H}=(\mathbf{F},\mathbf{G})$ the tensor of fluxes in the x and y directions, respectively:

$$\mathbf{U}=\begin{bmatrix}\eta\\ uh\\ vh\end{bmatrix} \qquad \mathbf{F}=\begin{bmatrix}uh\\ u^2h+\frac{1}{2}g(\eta^2-2\eta z)\\ uvh\end{bmatrix} \qquad \mathbf{G}=\begin{bmatrix}vh\\ uvh\\ v^2h+\frac{1}{2}g(\eta^2-2\eta z)\end{bmatrix} \quad (7)$$

The bed slope source term ($\mathbf{S}_0$) and porosity non-conservative product ($\mathbf{S}_p$) are defined as:

$$\mathbf{S}_0 = \begin{bmatrix} 0 \\ -g\eta\dfrac{\partial z}{\partial x} \\ -g\eta\dfrac{\partial z}{\partial y} \end{bmatrix} \qquad \mathbf{S}_p = \begin{bmatrix} -\dfrac{h}{\phi}\left(u\dfrac{\partial \phi}{\partial x} + v\dfrac{\partial \phi}{\partial y}\right) \\ -\dfrac{uh}{\phi}\left(u\dfrac{\partial \phi}{\partial x} + v\dfrac{\partial \phi}{\partial y}\right) \\ -\dfrac{vh}{\phi}\left(u\dfrac{\partial \phi}{\partial x} + v\dfrac{\partial \phi}{\partial y}\right) \end{bmatrix} \tag{8}$$

The non-conservative product $\mathbf{S}_p$ is discretized using a centered approximation. The contributions $\mathbf{S}_{p_{i_1}}$, $\mathbf{S}_{p_{i_2}}$, $\mathbf{S}_{p_{i_3}}$ adopted for updating the first, second and third conserved variables, respectively, are evaluated as follows:

$$\begin{aligned} \mathbf{S}_{p_{i_1}} &= -\frac{1}{\phi_i}\left(\overline{uh}_i \cdot \frac{\phi_{i+1} - \phi_{i-1}}{2\Delta x} + \overline{vh}_i \cdot \frac{\phi_{j+1} - \phi_{j-1}}{2\Delta y}\right) \\ \mathbf{S}_{p_{i_2}} &= -\frac{\overline{uh}_i}{\phi_i}\left(\frac{\overline{uh}_i}{\bar{h}_{i,x}} \cdot \frac{\phi_{i+1} - \phi_{i-1}}{2\Delta x} + \frac{\overline{vh}_i}{\bar{h}_{i,y}} \cdot \frac{\phi_{j+1} - \phi_{j-1}}{2\Delta y}\right) \\ \mathbf{S}_{p_{i_3}} &= -\frac{\overline{vh}_i}{\phi_i}\left(\frac{\overline{uh}_i}{\bar{h}_{i,x}} \cdot \frac{\phi_{i+1} - \phi_{i-1}}{2\Delta x} + \frac{\overline{vh}_i}{\bar{h}_{i,y}} \cdot \frac{\phi_{j+1} - \phi_{j-1}}{2\Delta y}\right) \end{aligned} \tag{9}$$

where, ϕ_i, $\phi_{i\text{-}1}$ and ϕ_{i+1} represent the porosity values of the considered cell (i), of its west (i-1) and east (i+1) neighboring one, and Δx and Δy denote the cell sizes along the x and y axis, respectively. The specific discharge $\overline{uh}_i$ and $\overline{vh}_i$, and water depths $\bar{h}_{i,x}$ and $\bar{h}_{i,y}$, which are referred to cell i, are evaluated as the averaged values of the reconstructed variables at the cell interfaces (in a first order scheme they will coincide with uh_i, vh_i, and h_i):

$$\overline{uh}_i = \frac{uh^R_{i-\frac{1}{2}} + uh^L_{i+\frac{1}{2}}}{2} \qquad \overline{vh}_i = \frac{vh^R_{j-\frac{1}{2}} + vh^L_{j+\frac{1}{2}}}{2} \tag{10}$$

$$\bar{h}_{i,x} = \frac{h^R_{i-\frac{1}{2}} + h^L_{i+\frac{1}{2}}}{2} \qquad \bar{h}_{i,y} = \frac{h^R_{j-\frac{1}{2}} + h^L_{j+\frac{1}{2}}}{2} \tag{11}$$

where, considering the reconstructed values at the internal interfaces of cell i, $uh^R_{i-\frac{1}{2}}$ and $h^R_{i-\frac{1}{2}}$, $uh^L_{i+\frac{1}{2}}$ and $h^L_{i+\frac{1}{2}}$, denote the specific discharge and water depth values along the x direction, at the west and east interface, respectively, whereas $vh^R_{j-\frac{1}{2}}$ and $h^R_{j-\frac{1}{2}}$, and $vh^L_{j+\frac{1}{2}}$ and $h^L_{j+\frac{1}{2}}$, represent the specific discharge and water depth values along the y direction, at the south and north interface, respectively.

The friction source term ($\mathbf{S}_f$), which includes the effects caused by buildings (i.e., reduced conveyance, preferential flow pathways, dead zones) is derived according to the following steps. Considering that building effects are anisotropic and that conveyance porosity is directionally dependent, the roughness resistance term is expressed in tensor form as follows:

$$\mathbf{S}_f = \mathbf{R} \cdot \mathbf{U} = \begin{bmatrix} 0 & 0 & 0 \\ 0 & R_{xx} & R_{xy} \\ 0 & R_{yx} & R_{yy} \end{bmatrix} \begin{bmatrix} \eta \\ uh \\ vh \end{bmatrix} \tag{12}$$

where **R** denotes a second order tensor [48] with principal directions of maximum and minimum conveyance *L* and *T*, and components R_L and R_T, respectively.

As shown in Figure 1-b, the principal directions *L*-*T* are rotated by α degrees against the model frame *x*-*y* and thus the **R** components derive from the transformation law of a second-order tensor [48]:

$$\begin{aligned} \mathbf{S}_f = \mathbf{R} \cdot \mathbf{U} &= \begin{bmatrix} 0 & 0 & 0 \\ 0 & \cos\alpha & -\sin\alpha \\ 0 & \sin\alpha & \cos\alpha \end{bmatrix} \begin{bmatrix} 0 & 0 & 0 \\ 0 & R_L & 0 \\ 0 & 0 & R_T \end{bmatrix} \begin{bmatrix} 0 & 0 & 0 \\ 0 & \cos\alpha & \sin\alpha \\ 0 & -\sin\alpha & \cos\alpha \end{bmatrix} \begin{bmatrix} \eta \\ uh \\ vh \end{bmatrix} = \\ &= \begin{bmatrix} 0 & 0 & 0 \\ 0 & R_L\cos^2\alpha + R_T\sin^2\alpha & (R_L - R_T)\cos\alpha\sin\alpha \\ 0 & (R_L - R_T)\cos\alpha\sin\alpha & R_L\sin^2\alpha + R_T\cos^2\alpha \end{bmatrix} \begin{bmatrix} \eta \\ uh \\ vh \end{bmatrix} \end{aligned} \tag{13}$$

Focusing on the α rotation between *L*-*T* and *x*-*y* frames, the conserved variables *uh* and *vh* become:

$$uh = q_x = q_L \cos\alpha - q_T \sin\alpha \tag{14}$$

$$vh = q_y = q_L \sin\alpha + q_T \cos\alpha \tag{15}$$

where q_L and q_T represent the specific discharge along the principal directions with maximum and minimum resistance.

Substituting Eq. (14)-(15) in the conserved variable vector of system (13), the friction term reduces to:

$$\mathbf{S}_f = \begin{bmatrix} 0 \\ R_L q_L \cos\alpha - R_T q_T \sin\alpha \\ R_L q_L \sin\alpha + R_T q_T \cos\alpha \end{bmatrix} \tag{16}$$

The contributions $R_L q_L$ and $R_T q_T$ derive from the Manning friction resistance formulation reported in system (5) and, according to the approach described in Sect. 1, they are computed using the components of the effective flow velocity within the channel contractions u_{eL} and u_{eT}, along the *L* and *T* direction, respectively:

$$R_L q_L = -gh\frac{n^2 u_{eL}\sqrt{{u_{eL}}^2 + {u_{eT}}^2}}{h^{4/3}} \qquad R_T q_T = -gh\frac{n^2 u_{eT}\sqrt{{u_{eL}}^2 + {u_{eT}}^2}}{h^{4/3}} \tag{17}$$

Then, introducing Eq. (2), which relates the effective velocity to the porosity conveyance parameter, the resistance terms in Eq. (17) become:

$$R_L q_L = -gh\frac{n^2\phi^2 u_L\sqrt{u^2 + v^2}}{\Psi_L^2 h^{4/3}} \qquad R_T q_T = -gh\frac{n^2\phi^2 u_T\sqrt{u^2 + v^2}}{\Psi_T^2 h^{4/3}} \tag{18}$$

Finally, substituting the terms in Eq. (18) into the friction resistance vector (16), the friction source term $\mathbf{S}_f$ results:

$$\mathbf{S}_f = \begin{bmatrix} 0 \\ -gh\dfrac{n^2\phi^2 u_L\sqrt{u^2+v^2}}{\Psi_L^2 h^{4/3}}\cos\alpha + gh\dfrac{n^2\phi^2 u_T\sqrt{u^2+v^2}}{\Psi_T^2 h^{4/3}}\sin\alpha \\ -gh\dfrac{n^2\phi^2 u_L\sqrt{u^2+v^2}}{\Psi_L^2 h^{4/3}}\sin\alpha - gh\dfrac{n^2\phi^2 u_T\sqrt{u^2+v^2}}{\Psi_T^2 h^{4/3}}\cos\alpha \end{bmatrix} \tag{19}$$

The friction term ($\mathbf{S}_f$), which adopts the Manning equation, is discretized according to the implicit formulation proposed in [51] that avoids spurious oscillations in the presence of small water depths. In the source term evaluation, the variables at the current time step n and at the incoming one n+1, are multiplied by an implicit coefficient β (here assumed equal to 0.5) according to the following relation:

$$\mathbf{S}_f = (1-\beta)\mathbf{S}_f^n + \beta\mathbf{S}_f^{n+1} \tag{20}$$

Therefore, after algebraic manipulations, the conserved variables at time n+1 are updated as follows:

$$\mathbf{U}_{i,j}^{n+1} = \mathbf{U}_{i,j}^n + \Delta t\left[\mathbf{I} - \frac{\Delta t}{2}\mathbf{Q}_f(\mathbf{U}_{i,j}^n)\right]^{-1}\mathbf{S}_f(\mathbf{U}_{i,j}^n) \tag{21}$$

where $\mathbf{I}$ is the identity matrix, and $\mathbf{Q}_f(\mathbf{U}_{i,j}^n)$ represents the Jacobian matrix of $\mathbf{S}_f(\mathbf{U}_{i,j}^n)$ that is evaluated as:

$$\mathbf{Q}_f(\mathbf{U}_{i,j}^n) = \begin{vmatrix} 0 & 0 & 0 \\ \dfrac{7}{3}S_{f_x} & -S_{f_x}\left(\dfrac{1}{u}+\dfrac{u}{u^2+v^2}\right) & -S_{f_x}\dfrac{v}{u^2+v^2} \\ \dfrac{7}{3}S_{f_y} & -S_{f_y}\dfrac{u}{u^2+v^2} & -S_{f_y}\left(\dfrac{1}{v}+\dfrac{v}{u^2+v^2}\right) \end{vmatrix} \tag{22}$$

The terms S_{f_x} and S_{f_y} in Eq. (22) are defined as:

$$S_{f_x} = \frac{gn^2\phi^2 uh\sqrt{uh^2+vh^2}}{\Psi_*^2 h^{10/3}} \qquad S_{f_y} = \frac{gn^2\phi^2 vh\sqrt{uh^2+vh^2}}{\Psi_*^2 h^{10/3}} \tag{23}$$

where Ψ_* corresponds to Ψ_L and Ψ_T when calculating the products $R_L q_L$ and $R_T q_T$ in Eq. (18), respectively.

The most relevant aspects of the 2D-SWE model and the related optimization techniques are here briefly recalled, as a detailed description is presented in [35–38] and it is beyond the scope of the present work. Dealing with a Finite Volume (FV) numerical scheme, the partial differential equations are solved on a structured Cartesian grid, but they can be easily extended to multi-resolution grids, such as the Block Uniform Quadtree ones [37]. The conserved variables $\mathbf{U}$ are reconstructed at the cell edges by means of the linear Monotone Upwind Schemes for Scalar

Conservation Laws (MUSCL) with minmod limiter [40], and thus a second order of accuracy in space is achieved.

In order to guarantee a robust treatment of wet-dry fronts, the flux correction of Kurganov and Petrova [52], which avoids the development of non-physical velocities with a zero-mass error, is adopted. Moreover, the implementation of the positivity-preserving hydrostatic reconstruction of Audusse et al. [53], and the additional slope source terms discretization proposed by Liang and Marche [54] ensure the *C-property* also in presence of wetting and drying fronts.

The numerical interface fluxes **F** and **G** are computed adopting the Harten, Lax and van Leer approximate Riemann solver with the Contact wave restored HLLC [50]. Finally, the conserved variables are updated at each time step, following the second order Runge-Kutta method that allows achieving a second order of accuracy in time.

In order to reduce the computational burden of classical 2D-SWE FV explicit schemes, the model is implemented in a CUDA/C++ code that exploits parallel computation offered by NVIDIA^{TM} GPUs [35].

3. Test cases

In this section, the proposed porosity model is tested by reproducing the flooding of three different synthetic urban environments. The first benchmark presents a regular and idealized building layout that allows assessing both the effective mesh-independence of the proposed numerical scheme and the feasibility to low-friction domains. The second test investigates if the proposed approach is able to describe the anisotropic effects of a residential urban district and the influence that walls and gardens have on the flood propagation. Finally, the model is tested against an experimental benchmark.

Each test case was performed adopting three different configurations:

1. R: Resolved buildings. The buildings are explicitly resolved over a fine mesh adopting a free-slip wall boundary condition. This method is known as “building hole” [10]. The results of this simulation are assumed as reference solution;
2. SP: single porosity (isotropic approach). In this case, urban zones are described by means of a unique storage/isotropic porosity parameter, ϕ, over a computational domain with a resolution lower than the one adopted for the above R approach;
3. AP: anisotropic porosity formulation. In this simulation, the proposed geometrical anisotropic porosity model is adopted (Eq.(5)). Urbanized areas are defined by means of a

storage porosity parameter ϕ, by two conveyance porosities, Ψ_L and Ψ_T, and by the rotation angle α. The mesh size is the same adopted for the SP case.

All the simulations were run on a NVIDIA ® Tesla ® P100 GPU.

3.1. Regular building urban layout

The first test case aims at assessing the capability and the advantages of the proposed anisotropic porosity scheme to reproduce the flood propagation in the idealized urban area shown in Figure 2, which is characterized by a regular building layout. Moreover, the application plans to stress that the results are independent from the mesh resolution and design, and not influenced by the adopted roughness coefficient.

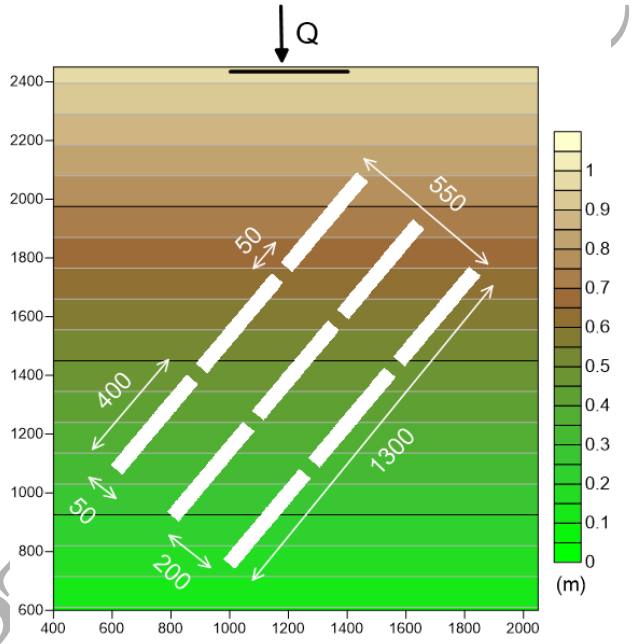

Figure 2. Regular building test. Bathymetry with the urban layout (dimensions in m).

The bottom slope is equal to 0.05% (southward) and the Manning roughness coefficient is firstly assumed as n = 0.02 $m^{-1/3}s$. A constant inflow discharge Q = 50 m^3/s is imposed as upstream boundary condition uniformly distributed along the central 400 m at the northern edge, whereas downstream (southern edge), a free outflow condition is adopted. At the beginning of the test, the domain is dry and the simulation ends once the steady state condition is achieved ($t \approx 10$ h).

The domain is discretized by means of a Cartesian grid, with cell size Δx = 2 m and Δx = 4 m for the reference (R) and porosity configurations (SP, AP), respectively. The geometrical parameters for the AP approach, together with the main features of the simulations, are reported in Table 1.

ID	Building modelling	Δx (m)	# cells (10^3)	t_{run} (min)	ϕ (-)	Ψ_L (-)	Ψ_T (-)	α (-)
R	Resolved	2	1052.05	24	-	-	-	-
SP	Porosity	4	263.53	3	0.748	-	-	-
AP	Porosity	4	263.53	3	0.748	0.727	0.077	50°

Table 1. Regular building test. ID, urban modelling approach, cell size Δx, number of cells, run time t_{run}, porosity parameter ϕ, anisotropic geometrical parameters Ψ_L, Ψ_T and angle α.

Figure 3 shows the water depths resulted at the end of the simulation. Assuming the resolved building results as reference solution (a), it emerges that the anisotropic scheme (c) is able to capture both the rise of the water depths caused by the buildings (red zone north-west) and the decrease at the back (blue zone south-east). Conversely, the isotropic approach does not reproduce the water depth distribution caused by the built area (b).

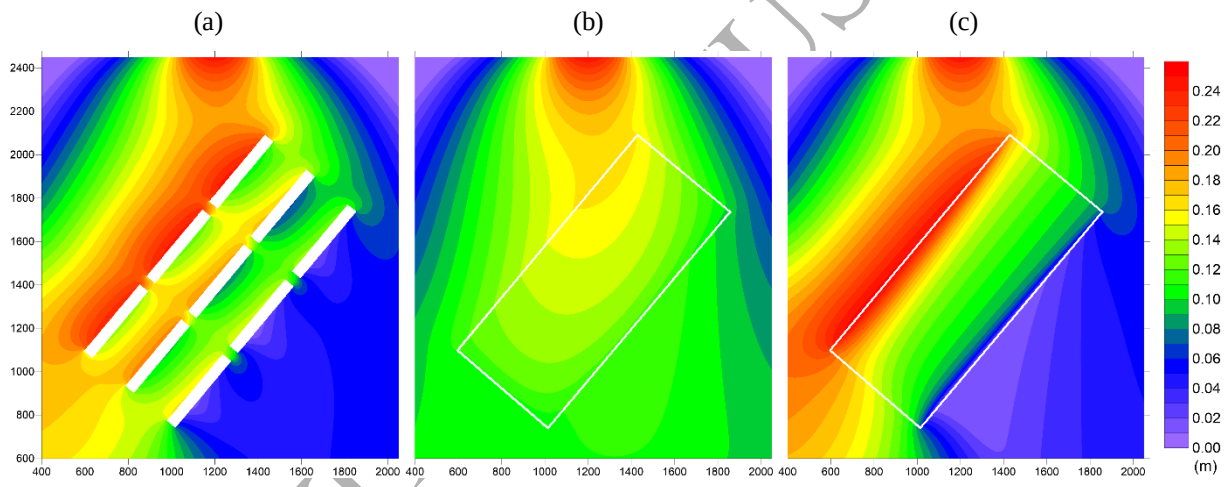

Figure 3. Regular building test. Resulted water depths for the (a) R, (b) SP and (c) AP configurations.

This behavior can be clearly distinguished looking at the velocity field illustrated in Figure 4. The isotropic scheme (b) does not describe the reduction in the available cross section, and thus the velocity vectors remain substantially straight across the urban area. Conversely, the anisotropic scheme (c) well captures both the velocity field in the four corners of the urban layout and the change in the direction of the velocity vectors. The only main differences with the reference solution are the zones where water enters and exits the streets of the urban district that obviously only a resolved scheme can capture.

(a) (b) (c)

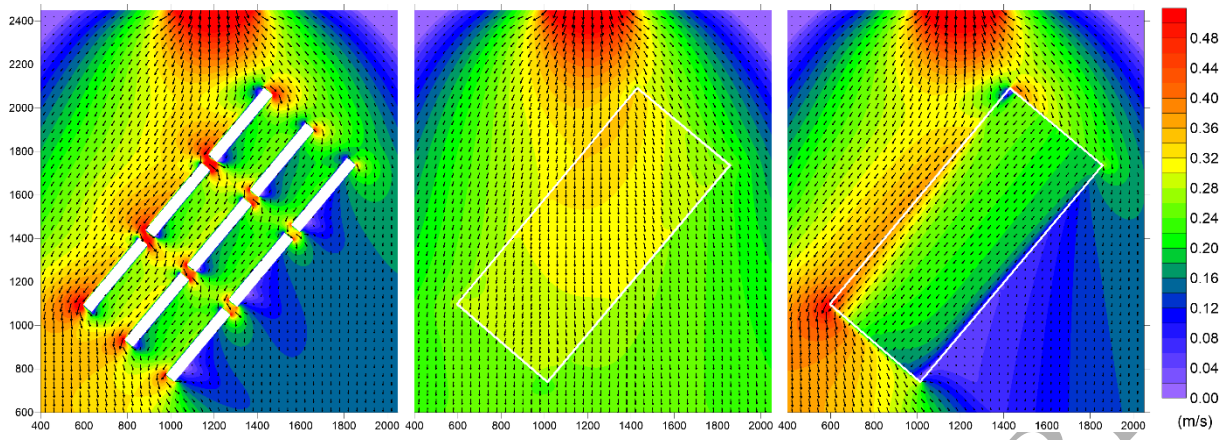

Figure 4. Regular building test. Resulted velocity field for the (a) R, (b) SP and (c) AP configurations.

A quantitative analysis of the results previously illustrated was performed by computing the L_2 error norm for the water depth and velocity variables, according to:

$$L_2(f) = \sqrt{\frac{1}{N}\sum_{i=1}^{N}\left[f_{por}^{i} - f_{res}^{i}\right]^2} \quad (24)$$

where N denotes the number of computational cells, f the variable of interest (water depth h and velocity components u and v), f_{por} the numerical solution obtained with the SP and AP approaches, respectively, and f_{res} the solution of the resolved building scheme.

As confirmed by the L_2 norm values reported in Table 2 (A5, A6), the anisotropic approach presents errors equal to 2.6, 1.7 and 2.2 times lower than the isotropic one, for water depth h and velocity components u and v, respectively.

Moreover, the advantage of adopting the anisotropic porosity scheme, in spite of a resolved building one, emerges from the runtimes reported in Table 1: for this benchmark, the adoption of the AP model has allowed a reduction of the run times of about 8 times (24 min/3 min), if compared to the R one.

Since the proposed scheme includes the anisotropic building effects in the friction losses, a sensitivity analysis to the roughness coefficient is performed in order to test the model with low-friction regimes. Indeed, according to Eq. (19), anisotropy in friction losses is lost in case of $n = 0$. Since the AP scheme aims at the modelling of urbanized areas where the roughness coefficient is always greater than zero, the following Manning values have been assumed: 0.01, 0.015, and 0.03 $m^{-1/3}$·s.

As highlighted by the L_2 norm values reported in Table 2 (simulations from A1 to A8), even if the AP velocity errors slightly increase by decreasing the roughness values, the ratio between the isotropic and anisotropic norms is substantially similar, thus confirming the advantages of the AP

scheme also in presence of low-friction areas. The good agreement between the anisotropic and refined results, assuming the lowest Manning coefficient of 0.01 $m^{-1/3}$·s, is shown in Figures 5 and 6 for water depths and velocity, respectively.

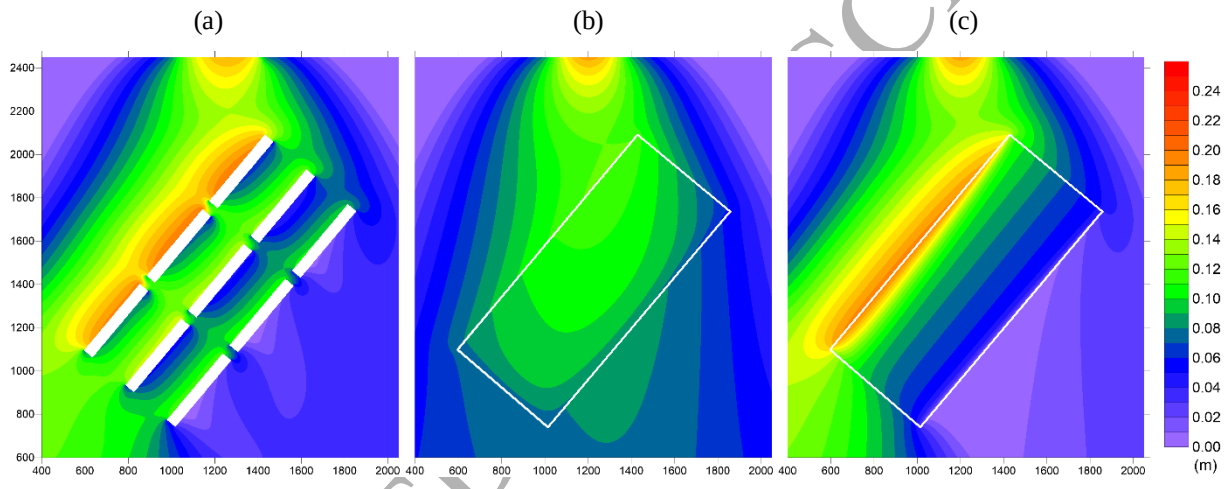

Figure 5. Regular building test with n=0.01 $m^{-1/3}$·s. Resulted water depths for the (a) R, (b) SP and (c) AP configurations.

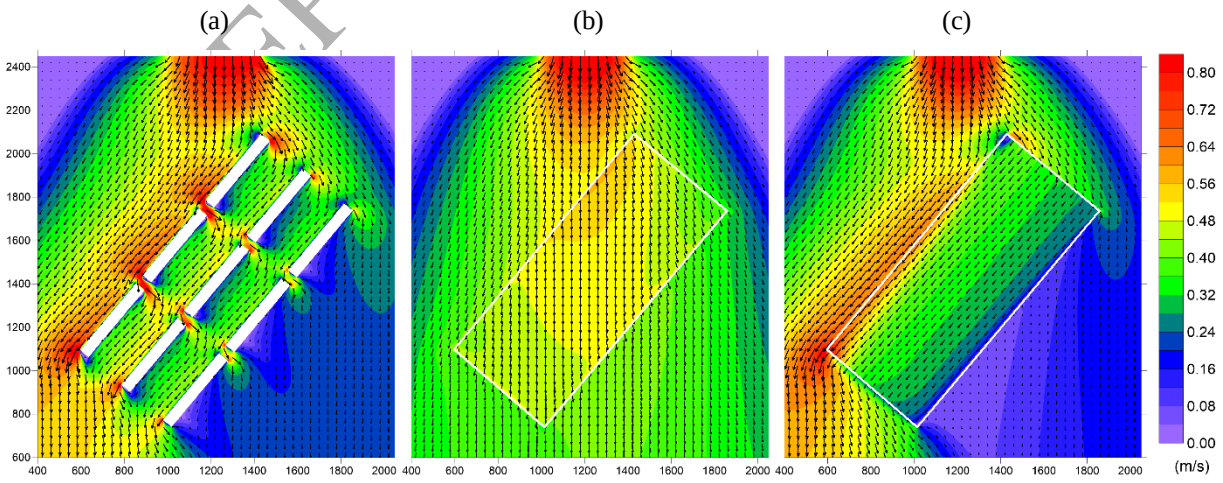

Figure 6. Regular building test with n=0.01 $m^{-1/3}$·s. Resulted velocity field for the (a) R, (b) SP and (c) AP configurations.

The second analysis concerns the adopted upstream boundary condition, thus keeping constant the mesh size (Δx = 2 m for the R configuration and 4 m for the SP and AP ones) and the roughness coefficient (n = 0.02 $m^{-1/3}$·s). The sensitivity to the inflow hydrograph is assessed by considering constant discharge values equal to 100 and 200 m^3/s, and the impulsive discharge wave shown in Figure 7 that derives from the dam-break of a reservoir with a volume of about $1 \cdot 10^6$ m^3.

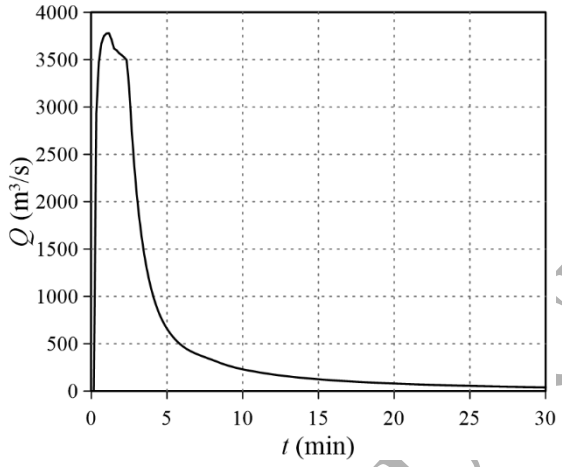

Figure 7. Regular building test with an impulsive inflow hydrograph. Upstream boundary condition.

The L_2 norms of the variables of interest, which for the dam-break case consist in the maximum water depth and velocity magnitude, are reported in Table 2 (simulations from B1 to B6). The ratio between the isotropic and anisotropic L_2 norms confirms that the proposed scheme performs up to 3.4 times better than the isotropic one.

With reference to the dam-break test (simulations B5-B6 in Table 2), Figures 8 and 9 compare the maximum water depth and velocity magnitude, respectively. The AP scheme is able to capture the rise of the water depth at the north-west corner of the urban layout (panel (c) in Figure 8) and the bore reflections that can be clearly distinguished in the velocity field of the refined simulation (panel (a) in Figures 8-9). Conversely, the SP model underestimates the reflection of the wave against the porous zone and overestimates the velocity field in the urbanized area (panel (b) in Figure 9).

(a) (b) (c)

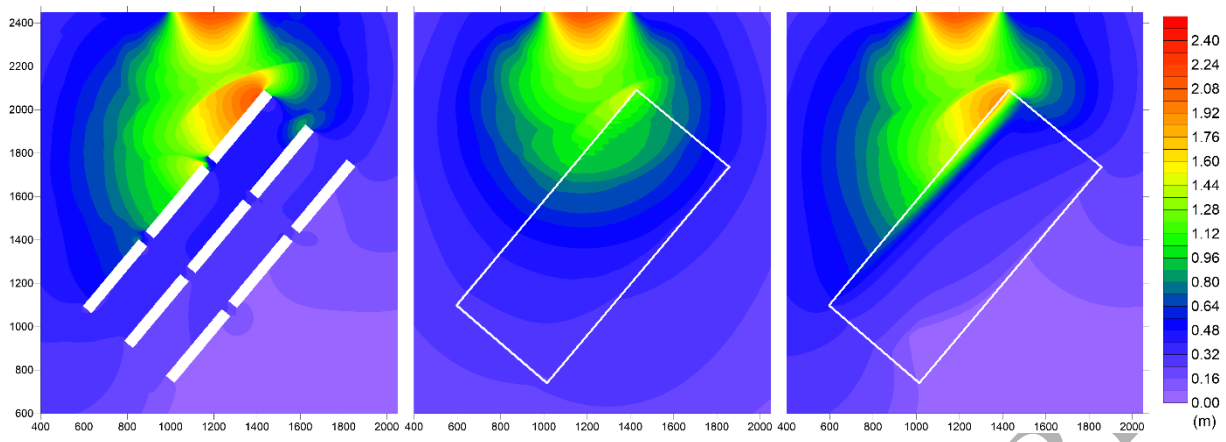

Figure 8. Regular building test with an impulsive inflow hydrograph. Maximum water depths for the (a) R, (b) SP and (c) AP configurations.

(a) (b) (c)

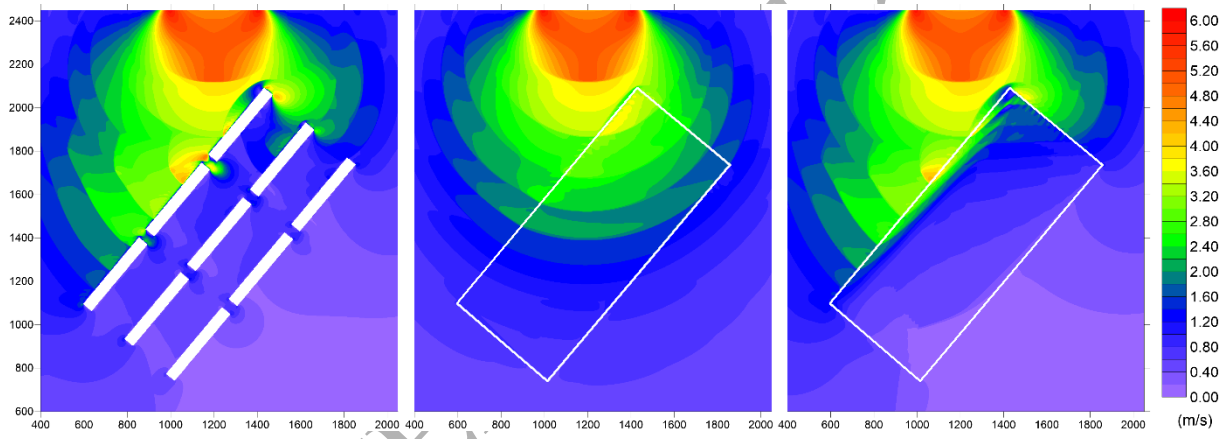

Figure 9. Regular building test with an impulsive inflow hydrograph. Maximum velocity field for the (a) R, (b) SP and (c) AP configurations.

For this severe inflow condition, the urban flooding simulations are also compared by quantifying a hydraulic hazard indicator that accounts for contemporary hydrostatic and dynamic loads. Thus, the maximum total force D is computed as follows [55]:

$$D = h\sqrt{1 + 2Fr^2} \quad (25)$$

where h denotes the water depth and Fr the Froude number.

According to the partition shown in Figure 10, four hazard ranks are defined as follows: low ($0 \leq D < 0.5$), medium ($0.5 \leq D < 1$), high ($1 \leq D < 1.5$) and very high ($D \geq 1.5$).

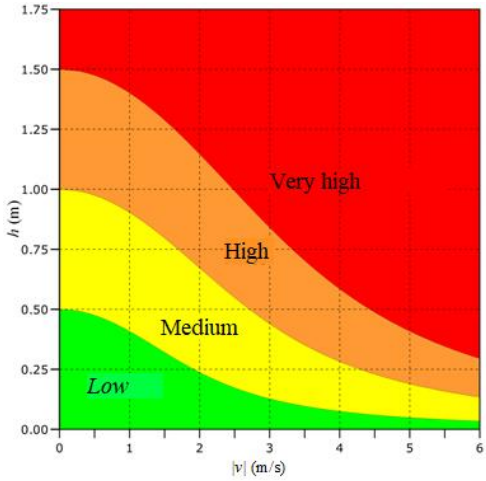

Figure 10. The h-|v| plane relating the maximum total force and the hazard degree.

Figure 11 compares the maximum total force values resulted for the three configurations. It is relevant to notice that the AP scheme (c) captures both the medium and high hazard degrees on the west edge of the urban layout and the low one inside the urban district. Conversely, the isotropic model (b) overestimates the hazard level in the urbanized area and underestimates it on the west side.

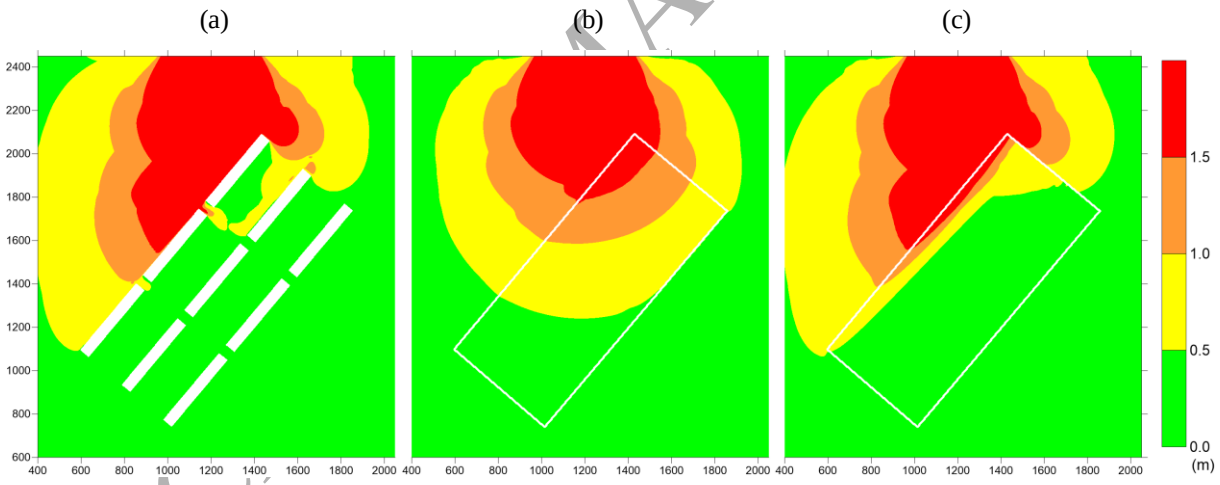

Figure 11. Regular building test with an impulsive inflow hydrograph. Maximum total force for the (a) R, (b) SP and (c) AP configurations.

The last analysis concerns the sensitivity of the proposed AP scheme to the mesh size and design. Focusing on the first issue, the test case (steady flow with Q = 50 m^3/s and n = 0.02 $m^{-1/3}\cdot s$) was further simulated by running the AP model on different grids with cell sizes of 2, 8, 15, 20, 40, and 80 m (simulations from C1 to C6 in Table 2).

According to the L_2 norms reported in Table 2, and to the maps of water depth and velocity shown in Figures 12-13, respectively, the results do not significantly change until Δx = 40 m.

Conversely, as can be expected, the adoption of Δx = 80 m determines an increase of the errors and a less adequate description of the flow field. Even if porosity models allow the adoption of coarser grids, the mesh size has to be small enough, compared with the length-scale of the problem, to represent the flow field variability well. Considering that the grid with Δx = 80 m does not fulfill this basic requirement, the analysis confirms that the proposed scheme is not oversensitive to the adopted mesh size.

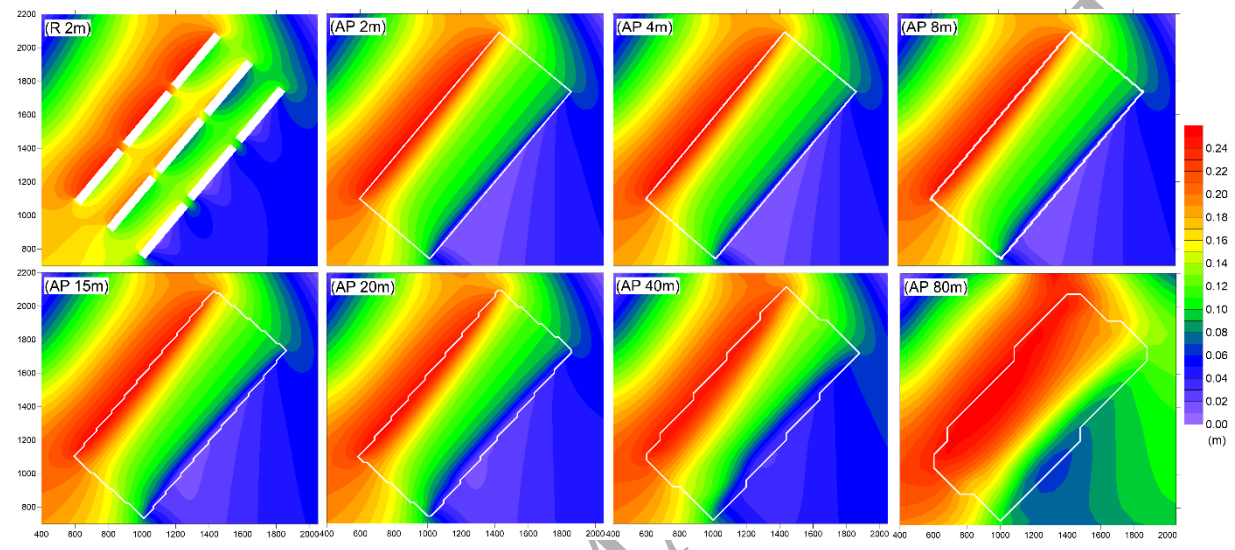

Figure 12. Regular building test. Resulted water depths for the R scheme with Δx=2 m, and the AP ones with Δx=2, 4, 8, 15, 20, 40 and 80 m, respectively.

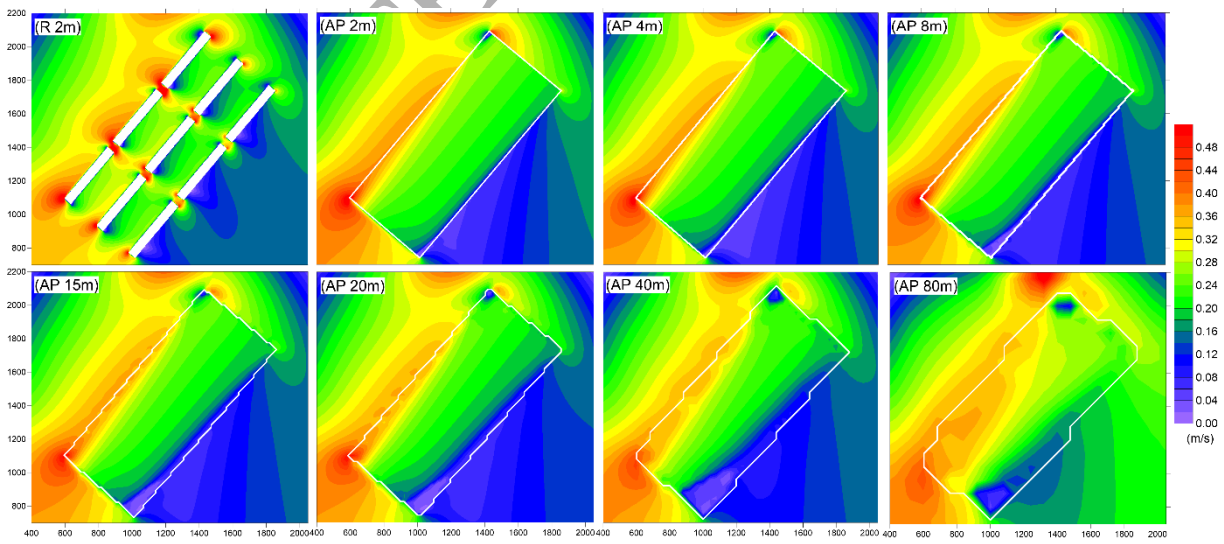

Figure 13. Regular building test. Resulted velocity field for the R scheme with Δx=2 m, and the AP ones with Δx=2, 4, 8, 15, 20, 40 and 80 m, respectively.

N	*n* ($m^{-1/3}\cdot s$)	Boundary condition	Δx (m)	ID	$\boldsymbol{L_2(h)}$ (m)	r(***h***) (-)	$\boldsymbol{L_2(u)}$ ($m\cdot s^{-1}$)	r(***u***) (-)	$\boldsymbol{L_2(v)}$ ($m\cdot s^{-1}$)	r(***v***) (-)
A1	0.01	50 m^3/s (constant)	4	SP	0.037		0.129		0.141	
A2				AP	0.016	2.4	0.071	1.8	0.075	1.9
A3	0.015	50 m^3/s (constant)	4	SP	0.041		0.097		0.099	
A4				AP	0.017	2.4	0.055	1.7	0.052	1.9
A5	0.02	50 m^3/s (constant)	4	SP	0.044		0.076		0.081	
A6				AP	0.017	2.6	0.046	1.7	0.037	2.2
A7	0.03	50 m^3/s (constant)	4	SP	0.050		0.059		0.060	
A8				AP	0.019	2.6	0.036	1.6	0.028	2.1
B1	0.02	100 m^3/s (constant)	4	SP	0.058		0.100		0.101	
B2				AP	0.020	2.9	0.059	1.7	0.045	2.2
B3	0.02	200 m^3/s (constant)	4	SP	0.079		0.131		0.131	
B4				AP	0.023	3.4	0.077	1.7	0.059	2.2
B5	0.02	dam-break	4	SP	0.184*		0.560**			
B6				AP	0.060*	3.1	0.185**	3.0		
C1	0.02	50 m^3/s (constant)	2	AP	0.017		0.047		0.037	
C2	0.02	50 m^3/s (constant)	8	AP	0.017		0.046		0.037	
C3	0.02	50 m^3/s (constant)	15	AP	0.018		0.048		0.040	
C4	0.02	50 m^3/s (constant)	20	AP	0.019		0.048		0.043	
C5	0.02	50 m^3/s (constant)	40	AP	0.021		0.054		0.047	
C6	0.02	50 m^3/s (constant)	80	AP	0.044		0.067		0.067	

*Table 2. Regular building test: L_2 norms with respect to the refined solution. Number of the simulation N, Manning coefficient n, upstream boundary condition, cell size Δx, ID, water depth norm $L_2(h)$, ratio between the SP and AP water depth norms r(h), u velocity component norm $L_2(u)$, ratio between the SP and AP u norms r(u), v velocity component norm $L_2(v)$, ratio between the SP and AP v norms r(v). For the simulations B5 and B6 * denotes the norms of the maximum water depth, and ** the norms of the maximum velocity magnitude.*

Finally, in order to test the independence of the AP approach to the mesh design, this regular benchmark was performed by counterclockwise rotating the domain of 45 degrees (Figure 14-a). Dealing with Cartesian grids, this rotation allows assessing the effects that the mesh design and orientation exert on the results of the presented approach. Figures 14 shows the comparison between the maps of water depth resulted from the AP simulations (Δx = 4 m), in the rotated (b) and original (c) configurations, respectively. Similarly, Figure 15 compares the velocity field maps for the simulations with (a) and without rotation (b). The results are almost identical to the ones showed in Figures 3-4 (also reported in a rotated framework in Figures 14-15 for the sake of comparison), confirming that the presented anisotropic approach is not influenced by the mesh orientation. It can thus be used with confidence also on structured grids.

This advantage is particularly important when using Cartesian or Block Uniform Quadtree grids [35–38], which in fact cannot provide the flexibility needed to meet the guidelines provided in [33] to limit oversensitivity to mesh design.

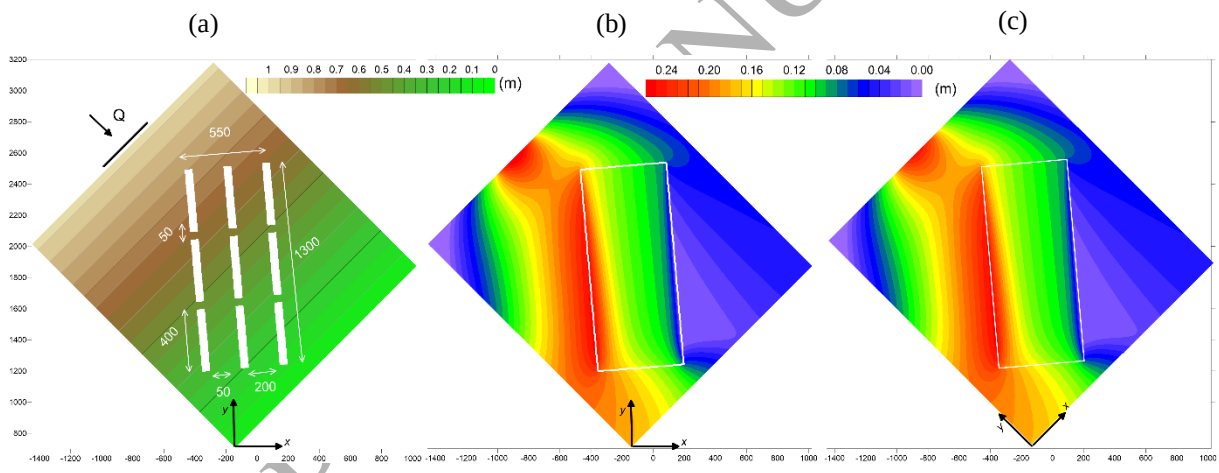

Figure 14. Bathymetry (a) and resulted water depths for the AP simulations in the rotated (b) and original (c) configurations.

(a) (b)

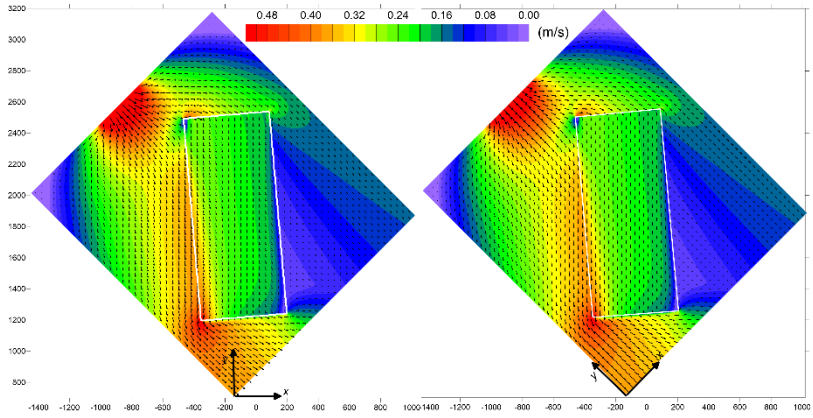

Figure 15. Resulted velocity field for the AP simulations in the rotated (a) and original (b) configurations.

3.2. Urban layout characterized by buildings with courtyards and gardens

The second application concerns the propagation of a flood wave in the idealized residential urbanized environment shown in Figure 16-a, that presents 24 detached/semi-detached houses. The houses are surrounded by gardens and courtyards, and they are separated one another by small walls, which are interrupted in a certain number of sections to reproduce the presence of gates. Practically, gardens can be viewed as spatially distributed storage areas that are flooded only by water entering the gates, and that negligibly contribute to conveyance. Thus, this idealized urban district emphasizes both the anisotropy in flow paths and the difference between storage and conveyance porosities. From geometrical considerations, while the storage porosity ϕ is close to unity, the conveyance porosity in the street direction, Ψ_L, is about 10 times smaller (Table 3).

The bottom slope is equal to 0.2% (southward) and the Manning roughness coefficient is assumed equal to 0.02 $m^{-1/3}s$. The initially dry urban district is flooded by a Gamma-distributed wave in the form:

$$Q(t) = B \cdot \frac{1}{k^b \Gamma(b)} t^{b-1} e^{-\frac{t}{k}} \tag{26}$$

where t represents the time, B the volume, $\Gamma(b)$ the gamma function with shape and scale parameters b and k, respectively. In the simulation, the following parameters were assumed: $B = 1.5 \cdot 10^6\ m^3$, $b = 5$, $k = 500$ s. The resulted inflow, which is prescribed as upstream boundary

condition normal to the central 300 m at the northern edge, approximately ends in 2 hours and presents a peak value of about 600 m^3/s (Figure 16-b). As downstream boundary condition (southern edge), a free outflow condition is imposed.

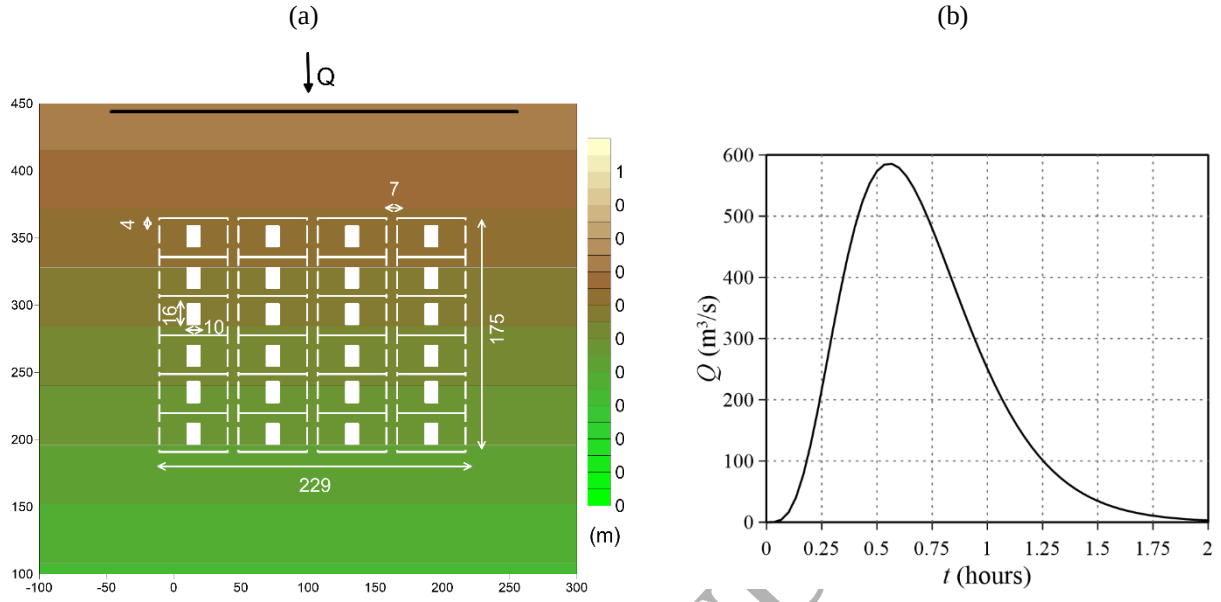

Figure 16. Buildings with courtyards test. (a) Urban layout (dimensions in m) and (b) inflow discharge.

Analogously to the first test, the flooding was modelled adopting a refined Cartesian grid (Δx = 0.5 m) with resolved buildings (R), a coarser grid (Δx = 2 m) with the single (SP) and the anisotropic (AP) porosity approaches. The geometrical parameters for the anisotropic approach, together with the main features of the simulations, are reported in Table 3.

ID	Building modelling	Δx (m)	# cells (10^6)	t_{run} (min)	ϕ (-)	Ψ_L (-)	Ψ_T (-)	α (-)
R	Resolved	0.5	3.96	74	-	-	-	-
SP	Porosity	2	0.25	1.5	0.904	-	-	-
AP	Porosity	2	0.25	1.5	0.904	0.0917	0.2743	90°

Table 3. Buildings with courtyards test. ID, urban modelling approach, cell size Δx, number of cells, run time t_{run}, porosity parameter ϕ, anisotropic geometrical parameters Ψ_L, Ψ_T and angle α.

The comparison of the maximum water depths (Figure 17) shows that the idealized residential district determines an upstream rise of the water depth (red zone in (a)) and a clear zone with very low water depths downstream of the built area. Assuming the refined simulation (a) as basis for comparison, the anisotropic porosity scheme (c) captures these two zones with different water depths significantly better than the isotropic one (b).

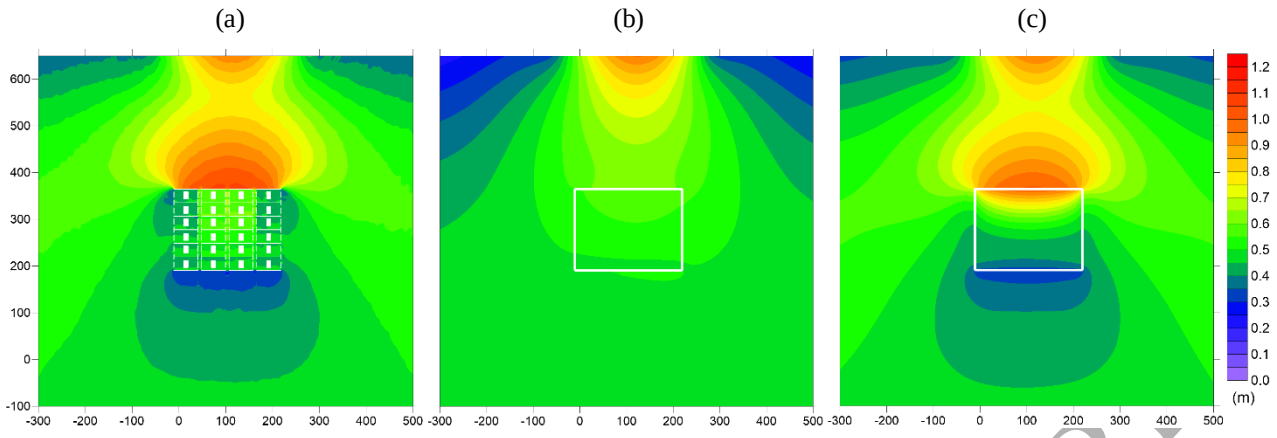

Figure 17. Buildings with courtyards test. Maximum water depths for the (a) R, (b) SP and (c) AP configurations.

Similarly, the comparison of the maximum resulted velocity field maps shown in Figure 18 confirms that the AP simulation well reproduces the deviation of the velocity vectors in the two upstream external corners of the urbanized area. As a result, the downstream stagnant area characterized by minimum velocity magnitude is properly captured. Obviously, the main velocity differences can be noticed at the entrance/exit of the principal vertical streets that actively conveys the flow, which only the refined solution (a) can reproduce. On the other side, the flow velocity distribution is not adequately reproduced by the SP solution, where the presence of the urban area does not sufficiently influence the flow field.

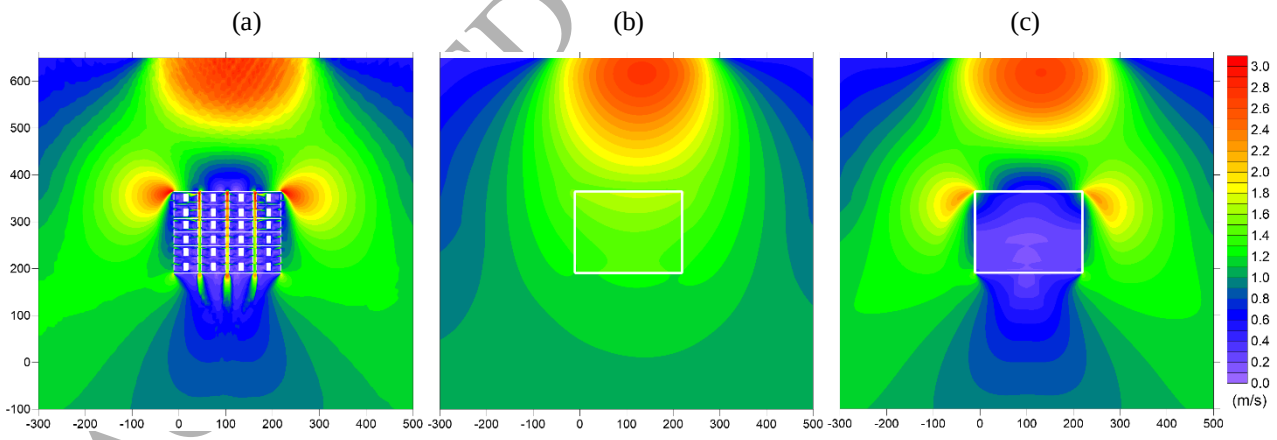

Figure 18. Buildings with courtyards test. Maximum velocity field for the (a) R, (b) SP and (c) AP configurations.

The resulted maximum total force maps shown in Figure 19 highlight that, if compared to the refined solution (a), the AP scheme (c) well captures both the upstream high hazard degree zone and the low one located downstream the urban area: the main difference is along the three vertical

streets. Conversely, the SP model overestimates the hazard degree in the urban zone and in the south portion of the domain.

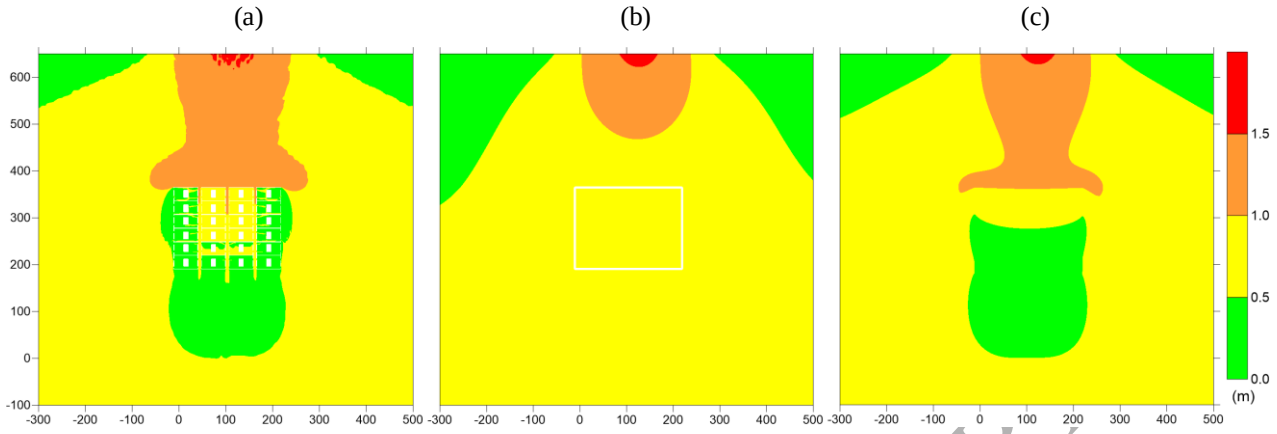

Figure 19. Buildings with courtyards test. Maximum total force for the (a) R, (b) SP and (c) AP configurations.

In order to quantitatively compare the differences between the reference/resolved solution and the porosity approaches, the L_2 norm error is evaluated according to Eq. (24), for the maximum water depth and velocity magnitude, respectively. The L_2 values reported in Table 4 highlight that the errors occurred adopting the AP approach are significantly lower than the ones obtained with an isotropic one.

ID	$L_2(h_{max})$ (m)	$r(h_{max})$ (-)	$L_2(\|\mathbf{v}\|_{max})$ (m)	$r(\|\mathbf{v}\|_{max})$ (-)
SP	0.101		0.338	
AP	0.039	2.6	0.153	2.2

Table 4. Buildings with courtyards test. L_2 norms for water depth and velocity magnitude.

Finally, focusing on the computational times reported in Table 3, it is relevant to notice that the anisotropic scheme, similarly to the isotropic one, allows reducing the runtimes by a factor of 50, if compared to the resolved simulation.

3.3. The Toce valley experimental flooding

The AP approach validation is finally assessed reproducing the Toce River experimental benchmark, which was carried out during the EU IMPACT project (Investigation of extreMe flood Processes And unCerTainty) in order to investigate the flooding of an urban environment. Since a detailed description of the laboratory facilities and benchmark characteristics can be found in

[56,57], and in many other works focusing on porosity schemes [14,20,23,45], only the most relevant information is here reported.

The physical model (scale 1:100) of the Toce valley (Northern Italy) includes an urban district that is modelled with square concrete building blocks of 15 cm. At the beginning of the experiment, the domain is dry and an inflow discharge is pumped for t = 60 s at the entrance of the river. Then the flood propagates in the valley crossing the houses, and the gauging points located in the domain register the water levels time histories.

The Toce River benchmark can be performed adopting various configurations, concerning the bathymetry (original, modified), the inflow discharge (low, medium, high) and the building layout (aligned, staggered). In the present work, the valley was assumed in its original configuration, with the checker board building layout shown in Figure 20-a. The Manning roughness coefficient was set equal to n = 0.0162 $m^{-1/3}s$ as reported in [56,57], and as upstream boundary condition the high discharge data set [56,57] was prescribed (Figure 20-b), whereas downstream a free outflow condition was specified at the end of the valley reach.

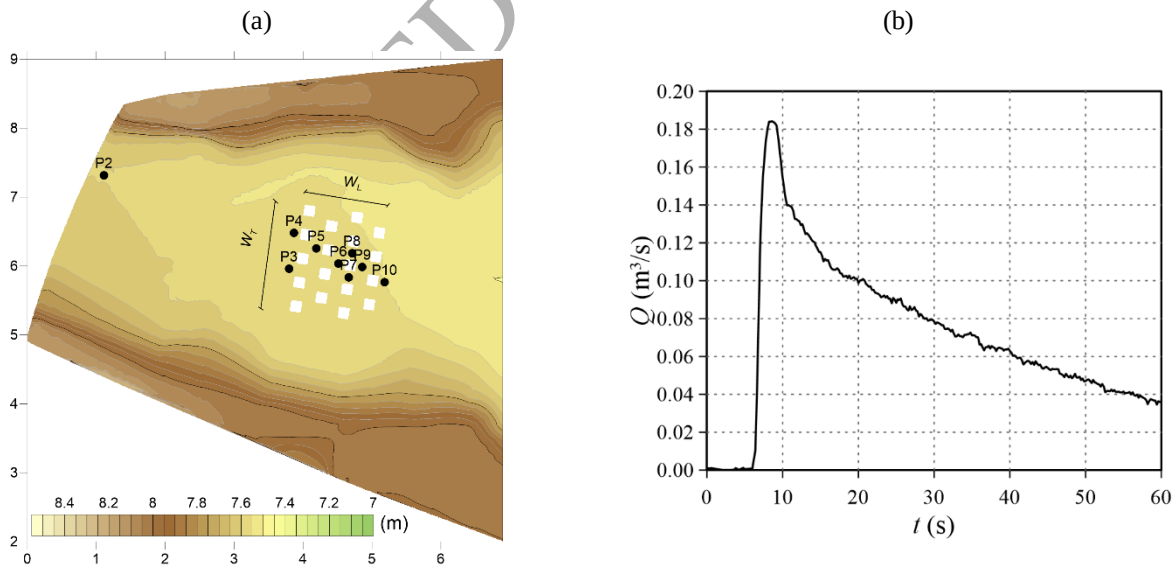

Figure 20. Toce River test. Original bathymetry and staggered urban layout with 18 buildings (a), where the gauging points are indicated, and inflow hydrograph (b).

The experimental test was simulated modelling the urban area with resolved building (R), and with the single (SP) and anisotropic porosity (AP) approaches. A Cartesian mesh discretized the domain with cells Δx = 1 cm and Δx = 5 cm for the refined and porosity configurations, respectively. The geometrical parameters for the anisotropic approach, together with the main feature of the simulations, are reported in Table 5. It is relevant to notice that for this staggered building configuration, the conveyance parameters, Ψ_L and Ψ_T, were calculated not simply considering the outer building row. Conversely, they were evaluated assuming the inner rows collapsing over the first one, which means that the inner buildings rigidly shift along the *L*-*T* principal directions:

$$\Psi_T = \frac{w}{W_T} = 1 - \frac{9 \cdot W_{obst}}{W_T} = 1 - \frac{9 \cdot 15}{155} = 0.129 \quad (27)$$

$$\Psi_L = \frac{w}{W_L} = 1 - \frac{4 \cdot W_{obst}}{W_L} = 1 - \frac{4 \cdot 15}{120} = 0.5 \quad (28)$$

where w is the width free of buildings, W_L and W_T the widths of the entire urbanized area along *L* and *T* directions, respectively, and W_{obst} is the width of a single obstacle (building block).

ID	Building modelling	Δx (cm)	# cells (10^3)	t_{run} (min)	ϕ (-)	Ψ_L (-)	Ψ_T (-)	α (-)
R	Resolved	1	345.51	6.9	-	-	-	-
SP	Porosity	5	13.89	0.5	0.782	-	-	-
AP	Porosity	5	13.89	0.5	0.782	0.5	0.129	82°

Table 5. Toce River test. ID, urban modelling approach, cell size Δx, number of cells, run time t_{run}, porosity parameter ϕ, anisotropic geometrical parameters Ψ_L, Ψ_T and angle α.

Figures 21-22 illustrate the flooding area at time t =14 s, in terms of water depth and velocity, respectively.

(a) (b) (c)

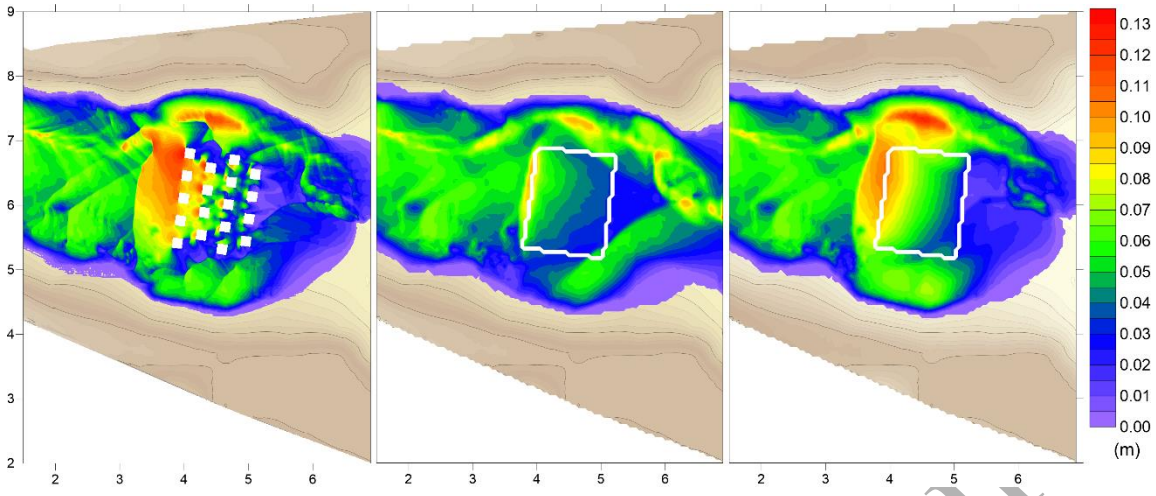

Figure 21. Toce River test. Water depths at t=14 s for the (a) R, (b) SP and (c) AP configurations. In background the bathymetry.

(a) (b) (c)

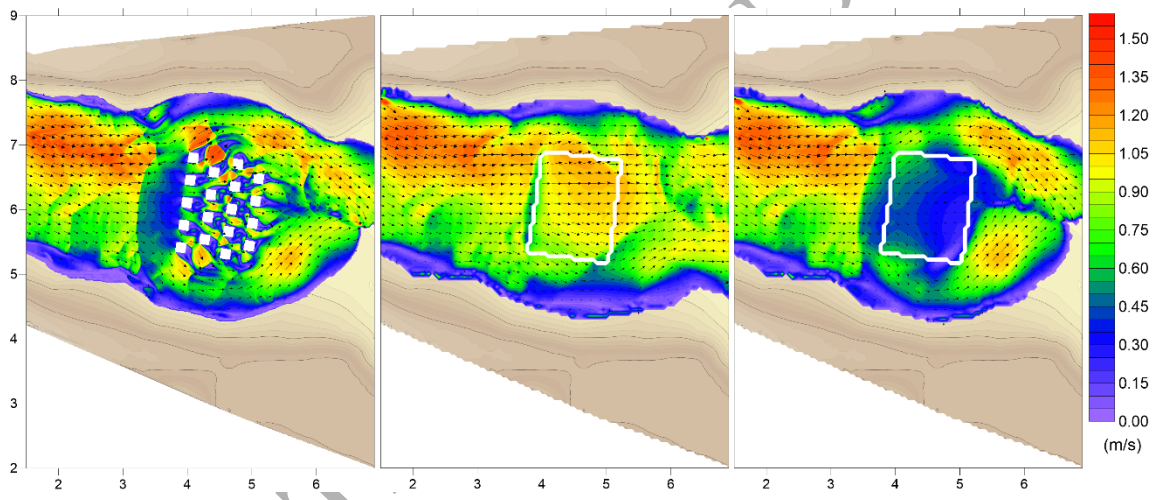

Figure 22. Toce River test. Velocity field at t=14 s for the (a) R, (b) SP and (c) AP configurations. In background the bathymetry.

As for the previous tests, the results of the refined mesh with resolved buildings (a) are assumed as reference solution. Focusing on the water depth maps (Figure 21), it emerges that the hydraulic jump that forms just upstream the obstacles is correctly reproduced by the AP configuration (c). Conversely, the water depths upstream the building region are significantly underestimated in the SP scheme (b). Due to underestimated flow resistances of the SP approach, the stagnant zone at the back of the urban district is better reproduced in the AP result (c) than in the SP (b) one. The variation of the flow field regime is further highlighted in the velocity maps of Figure 22. The urban area determines the transition from supercritical to subcritical flow conditions: between the two adopted porosity approaches, the AP scheme (c) better reproduces this effect than the SP one (b).

Dealing with an experimental benchmark, a further validation is assessed by comparing the results of the three simulations with the water level time histories [56,57] recorded at the gauges illustrated in Figure 20-a; the comparison between registered and simulated water levels is shown in Figure 23. The water levels at gauge P2, which is located at the entrance of the valley, are identical in the three configurations, since they are not influenced by the urban zone (small differences are only ascribed to the mesh size). Focusing on the urbanized area, gauges P3 and P4, which lay in front of the houses, provide information about the dam break wave impacting on the buildings. The trends confirm that the isotropic porosity approach significantly underestimates the reflection of the flood wave against the obstacles and the consequent level rise. Conversely, the anisotropic porosity results are closer to the resolved ones and, above all, to the experimental data set. The AP scheme better captures the trend also at the gauge P5, which is located in front of a building along the second row of obstacles, than the R and SP models. Gauges P6, P7, P8, and P9 are located around a building in the middle of the urban zone. For these gauges, the isotropic scheme always underestimates the experimental data, whereas the anisotropic results are similar to the refined one and better agree with the recorded levels than the SP ones. The last considered gauge, P10, which is on the wake of the last obstacle row, describes the effects of blocks at the back of the urban area. Between the two porosity configurations, the anisotropic results are closer to the experimental data than the other one.

Finally, it is relevant to highlight, also for this last benchmark, the reduction of the computational times that is achieved using the porosity approach. Both the SP and AP simulations (Table 5) reduced the runtimes by a factor of 14, if compared to the resolved configurations. However, between the two porosity approaches, the anisotropic scheme is the only one that has the capability of reproducing the experimental test similarly to the resolved one.

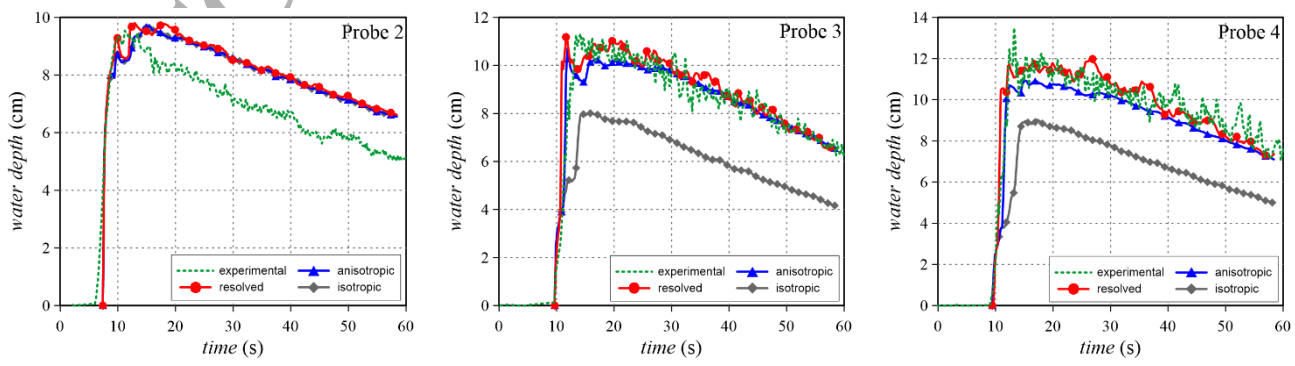

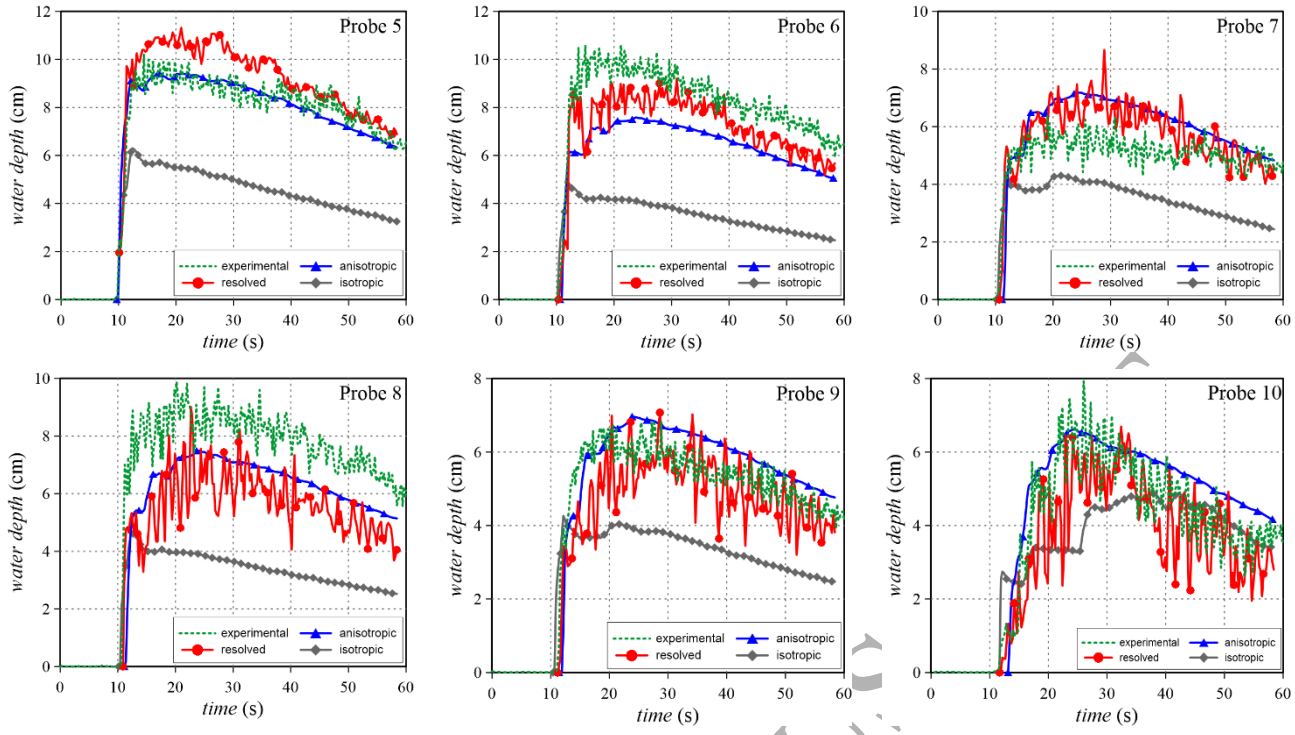

Figure 23. Toce River test. Comparison between registered and simulated water levels at the gauges.

4. Conclusions

With the aim of capturing the effects exerted by buildings and obstacles in the flooding of urbanized areas, the present paper concerned the implementation of an anisotropic scheme in a well-balanced formulation solving the 2D-SWEs with porosity on structured grids. In the model, a standard isotropic porosity accounts for reduction in mass and momentum storage due to buildings, whereas anisotropy related to street grid and building alignment is modeled through a directionally dependent, tensor formulation of the friction losses.

The model assessment showed the capability of the proposed scheme to reproduce the flooding in urbanized areas with a reduction of the run times up to 50 with respect to a high-resolution resolved simulation (depending on the test case). The scheme performs well for a wide range of bottom roughness parameters and is not oversensitive to the mesh resolution and design.

Since the conveyance calculation presented in the paper lays on simple geometrical considerations, future work should focus on the definition of porosity parameters in the framework of real urban districts with complex building layout and street networks.

Acknowledgments

This work was partially supported by Ministry of Education, Universities and Research under the Scientific Independence of young Researchers project, grant number RBSI14R1GP, CUP code D92I15000190001. This research benefits from the HPC (High Performance Computing) facility of the University of Parma, Italy. The authors are grateful to the editor and the anonymous reviewers for the valuable suggestions on the early version of this manuscript.

References

[1] Yu D, Lane SN. Urban fluvial flood modelling using a two-dimensional diffusion-wave treatment. Part 2: development of a sub-grid-scale treatment. Hydrol Process 2006;20:1567–83. doi:10.1002/hyp.5936.

[2] Yu D, Lane SN. Interactions between subgrid-scale resolution, feature representation and grid-scale resolution in flood inundation modelling. Hydrol Process 2011;25:36–53. doi:10.1002/hyp.7813.

[3] Sanders BF. Hydrodynamic Modeling of Urban Flood Flows and Disaster Risk Reduction. Oxford Res Encycl Nat Hazard Sci 2017:1–22. doi:10.1093/acrefore/9780199389407.013.127.

[4] Guinot V, Sanders BF, Schubert JE. Dual integral porosity shallow water model for urban flood modelling. Adv Water Resour 2017;103:16–31. doi:10.1016/j.advwatres.2017.02.009.

[5] Schubert JE, Sanders BF, Smith MJ, Wright NG. Unstructured mesh generation and landcover-based resistance for hydrodynamic modeling of urban flooding. Adv Water Resour 2008;31:1603–21. doi:10.1016/j.advwatres.2008.07.012.

[6] Tsubaki R, Fujita I. Unstructured grid generation using LiDAR data for urban flood inundation modelling. Hydrol Process 2010;24:1404–20. doi:10.1002/hyp.7608.

[7] Dottori F, Todini E. Testing a simple 2D hydraulic model in an urban flood experiment. Hydrol Process 2013;27:1301–20. doi:10.1002/hyp.9370.

[8] McMillan HK, Brasington J. Reduced complexity strategies for modelling urban floodplain inundation. Geomorphology 2007;90:226–43. doi:10.1016/j.geomorph.2006.10.031.

[9] Petaccia G, Soares-Frazão S, Savi F, Natale L, Zech Y. Simplified versus Detailed Two-

Dimensional Approaches to Transient Flow Modeling in Urban Areas. J Hydraul Eng 2010;136:262–6. doi:10.1061/(ASCE)HY.1943-7900.0000154.

[10] Schubert JE, Sanders BF. Building treatments for urban flood inundation models and implications for predictive skill and modeling efficiency. Adv Water Resour 2012;41:49–64. doi:10.1016/j.advwatres.2012.02.012.

[11] Braschi G, Gallati M. Simulation of a levee-breaking submersion of planes and urban areas. HYDROCOMP '89, Proc. Int. Conf. Comput. Model. Exp. Methods Hydraul., N. Y.: Elsevier Applied Sci.; 1989, p. 117–26.

[12] Defina A, D'Alpaos L, Matticchio B. A new set of equations for very shallow water and partially dry areas suitable to 2D numerical models. In: Molinaro P, Natale L, editors. Model. Flood Propag. Over Initial. Dry Areas., New York: American Society of Civil Engineers; 1994, p. 72–81.

[13] Olsen NRB, Stokseth S. Three-dimensional numerical modelling of water flow in a river with large bed roughness. J Hydraul Res 1995;33:571–81. doi:10.1080/00221689509498662.

[14] Guinot V, Soares-Frazão S. Flux and source term discretization in two-dimensional shallow water models with porosity on unstructured grids. Int J Numer Methods Fluids 2006;50:309–45. doi:10.1002/fld.1059.

[15] Cea L, Vázquez-Cendón ME. Unstructured finite volume discretization of two-dimensional depth-averaged shallow water equations with porosity. Int J Numer Methods Fluids 2010;62:903–30. doi:10.1002/fld.2107.

[16] Chen AS, Evans B, Djordjević S, Savić DA. A coarse-grid approach to representing building blockage effects in 2D urban flood modelling. J Hydrol 2012;426–427:1–16. doi:10.1016/j.jhydrol.2012.01.007.

[17] Chen AS, Evans B, Djordjević S, Savić DA. Multi-layered coarse grid modelling in 2D urban flood simulations. J Hydrol 2012;470–471:1–11. doi:10.1016/j.jhydrol.2012.06.022.

[18] Ferrari A, Vacondio R, Dazzi S, Mignosa P. A 1D–2D Shallow Water Equations solver for discontinuous porosity field based on a Generalized Riemann Problem. Adv Water Resour

2017;107:233–49. doi:10.1016/j.advwatres.2017.06.023.

[19] Finaud-Guyot P, Delenne C, Lhomme J, Guinot V, Llovel C. An approximate-state Riemann solver for the two-dimensional shallow water equations with porosity. Int J Numer Methods Fluids 2010;62:1299–331. doi:10.1002/fld.2066.

[20] Soares-Frazao S, Lhomme J, Guinot V, Zech Y. Two-dimensional shallow-water model with porosity for urban flood modelling. J Hydraul Res 2008;46:45–64. doi:10.1080/00221686.2008.9521842.

[21] Testa G, Di Filippo A, Ferrari F, Gatti D, Pacheco R. Two-dimensional model for flood simulation over flat dry areas with infrastructures. In: Babovic V, Larsen LC, editors. Proc. Third Int. Conf. Hydroinformatics, Copenhagen: Balkema, Rotterdam; 1998, p. 231–8.

[22] Velickovic M, van Emelen S, Zech Y, Soares-Frazão S. Shallow-water model with porosity: sensitivity analysis to head losses and porosity distribution. River Flow 2010 Proc Int Conf Fluv Hydraul 2010:613–20.

[23] Sanders BF, Schubert JE, Gallegos HA. Integral formulation of shallow-water equations with anisotropic porosity for urban flood modeling. J Hydrol 2008;362:19–38. doi:10.1016/j.jhydrol.2008.08.009.

[24] Mignot E, Paquier A, Haider S. Modeling floods in a dense urban area using 2D shallow water equations. J Hydrol 2006;327:186–99. doi:10.1016/j.jhydrol.2005.11.026.

[25] Bruwier M, Mustafa A, Aliaga DG, Archambeau P, Erpicum S, Nishida G, et al. Influence of urban pattern on inundation flow in floodplains of lowland rivers. Sci Total Environ 2018;622–623:446–58. doi:10.1016/j.scitotenv.2017.11.325.

[26] Arrault A, Finaud-Guyot P, Archambeau P, Bruwier M, Erpicum S, Pirotton M, et al. Hydrodynamics of long-duration urban floods: experiments and numerical modelling. Nat Hazards Earth Syst Sci 2016;16:1413–29. doi:10.5194/nhess-16-1413-2016.

[27] Bruwier M, Archambeau P, Erpicum S, Pirotton M, Dewals B. Shallow-water models with anisotropic porosity and merging for flood modelling on Cartesian grids. J Hydrol 2017;554:693–709. doi:10.1016/j.jhydrol.2017.09.051.

[28] Özgen I, Liang D, Hinkelmann R. Shallow water equations with depth-dependent anisotropic porosity for subgrid-scale topography. Appl Math Model 2015;40(17--18):7447–73. doi:10.1016/j.apm.2015.12.012.

[29] Özgen I, Zhao J, Liang D, Hinkelmann R. Urban flood modeling using shallow water equations with depth-dependent anisotropic porosity. J Hydrol 2016;541:1165–84. doi:10.1016/j.jhydrol.2016.08.025.

[30] Kim B, Sanders B, Famiglietti JS, Guinot V. Urban flood modeling with porous shallow-water equations: A case study of model errors in the presence of anisotropic porosity. J Hydrol 2015;523:680–92. doi:10.1016/j.jhydrol.2015.01.059.

[31] Guinot V. A critical assessment of flux and source term closures in shallow water models with porosity for urban flood simulations. Adv Water Resour 2017;109:133–57. doi:10.1016/j.advwatres.2017.09.002.

[32] Defina A. Two-dimensional shallow flow equations for partially dry areas. Water Resour Res 2000;36:3251. doi:10.1029/2000WR900167.

[33] Guinot V. Consistency and bicharacteristic analysis of integral porosity shallow water models. Explaining model oversensitivity to mesh design. Adv Water Resour 2017;107:43–55. doi:10.1016/j.advwatres.2017.06.008.

[34] Liang Q, Borthwick AGL. Adaptive quadtree simulation of shallow flows with wet–dry fronts over complex topography. Comput Fluids 2009;38:221–34. doi:10.1016/j.compfluid.2008.02.008.

[35] Vacondio R, Dal Palù A, Mignosa P. GPU-enhanced Finite Volume Shallow Water solver for fast flood simulations. Environ Model Softw 2014;57:60–75. doi:10.1016/j.envsoft.2014.02.003.

[36] Vacondio R, Aureli F, Ferrari A, Mignosa P, Dal Palù A. Simulation of the January 2014 flood on the Secchia River using a fast and high-resolution 2D parallel shallow-water numerical scheme. Nat Hazards 2016;80:103–25. doi:10.1007/s11069-015-1959-4.

[37] Vacondio R, Dal Palù A, Ferrari A, Mignosa P, Aureli F, Dazzi S. A non-uniform efficient

grid type for GPU-parallel Shallow Water Equations models. Environ Model Softw 2017;88:119–37. doi:10.1016/j.envsoft.2016.11.012.

[38] Dazzi S, Vacondio R, Dal Palù A, Mignosa P. A local time stepping algorithm for GPU-accelerated 2D shallow water models. Adv Water Resour 2018;111:274–88. doi:10.1016/j.advwatres.2017.11.023.

[39] Velickovic M, Zech Y, Soares-Frazão S. Steady-flow experiments in urban areas and anisotropic porosity model. J Hydraul Res 2017;55:85–100. doi:10.1080/00221686.2016.1238013.

[40] Toro EF. Riemann Solvers and Numerical Methods for Fluid Dynamics. Springer; 1999.

[41] Murillo J, García-Navarro P. Augmented versions of the HLL and HLLC Riemann solvers including source terms in one and two dimensions for shallow flow applications. J Comput Phys 2012;231:6861–906. doi:10.1016/j.jcp.2012.06.031.

[42] Guinot V, Delenne C, Rousseau A, Boutron O. Flux closures and source term models for shallow water models with depth-dependent integral porosity. Adv Water Resour 2018;122:1–26. doi:10.1016/j.advwatres.2018.09.014.

[43] Viero DP, Susin FM, Defina A. A note on weak shock wave reflection. Shock Waves 2013;23:505–11. doi:10.1007/s00193-013-0452-9.

[44] Defina A, Susin FM, Viero DP. Numerical study of the Guderley and Vasilev reflections in steady two-dimensional shallow water flow. Phys Fluids 2008;20:097102. doi:10.1063/1.2972936.

[45] Guinot V. Multiple porosity shallow water models for macroscopic modelling of urban floods. Adv Water Resour 2012;37:40–72. doi:10.1016/j.advwatres.2011.11.002.

[46] Viero DP. Modelling urban floods using a finite element staggered scheme with an anisotropic dual porosity model. J Hydrol 2019;568:247–59. doi:10.1016/j.jhydrol.2018.10.055.

[47] Defina A, Viero DP. Open channel flow through a linear contraction. Phys Fluids 2010;22:036602. doi:10.1063/1.3370334.

[48] Viero DP, Valipour M. Modeling anisotropy in free-surface overland and shallow inundation flows. Adv Water Resour 2017;104:1–14. doi:10.1016/j.advwatres.2017.03.007.

[49] Abgrall R, Karni S. A comment on the computation of non-conservative products. J Comput Phys 2010;229:2759–63. doi:10.1016/j.jcp.2009.12.015.

[50] Toro EF. Shock-capturing methods for free-surface shallow flows. John Wiley; 2001.

[51] Caleffi V, Valiani A, Zanni A. Finite volume method for simulating extreme flood events in natural channels. J Hydraul Res 2003;41:167–77. doi:10.1080/00221680309499959.

[52] Kurganov A, Petrova G. A second-order well-balanced positivity preserving central-upwind scheme for the Saint-Venant system. Commun Math Sci 2007;5:133–60. doi:10.4310/CMS.2007.v5.n1.a6.

[53] Audusse E, Bouchut F, Bristeau M-O, Klein R, Perthame B. A Fast and Stable Well-Balanced Scheme with Hydrostatic Reconstruction for Shallow Water Flows. SIAM J Sci Comput 2004;25:2050–65. doi:10.1137/S1064827503431090.

[54] Liang Q, Marche F. Numerical resolution of well-balanced shallow water equations with complex source terms. Adv Water Resour 2009;32:873–84. doi:10.1016/j.advwatres.2009.02.010.

[55] Aureli F, Maranzoni A, Mignosa P, Ziveri C. 2D numerical modelling for hydraulic hazard assessment: a dam-break case study. In: Altinakar M, Kokpinar MA, Darama Y, Yegen B, Harmancioglu NB, editors. River Flow 2008, Proc. Int. Conf. Fluv. Hydraul., Cesme, Izmir, Turkey: Kubaba; 2008, p. 729–36.

[56] Alcrudo F, Garcia-Navarro P, Brufau P, Murillo J, Garcia D, Mulet J, et al. The Model City Flooding Experiment. Proc. 2nd Proj. Work. EC Contract EVG1-CT-2001-00037 IMPACT Investig. Extrem. Flood Process. Uncertain., Mo i Rana (Norway): 2002, p. 17.

[57] Testa G, Zuccalà D, Alcrudo F, Mulet J, Soares-Frazão S. Flash flood flow experiment in a simplified urban district. J Hydraul Res 2007;45:37–44. doi:10.1080/00221686.2007.9521831.